

# The Sensorium Manifold:

## Native Multimodality via Isomorphism

Daniel Owen van Dommelen

*Independent Research - WORKING DRAFT*

[theapemachine@gmail.com](mailto:theapemachine@gmail.com)

February 5, 2026

### Abstract

We introduce the *Sensorium Manifold*, a thermodynamic computing substrate that replaces the autoregressive paradigm with global energy minimization. Current AI models rely on serial token generation and backpropagation-based optimization. We propose a system governed by *Hamiltonian dynamics*, where data is represented as a field of coupled oscillators and learning is the emergence of stable structure in an  $\omega$ -space hydrodynamic field  $\Psi(\omega)$ .

We introduce the *Universal Tokenizer*, a modality-agnostic input mechanism that maps raw bytes and sequence indices to unique oscillator frequencies via hashing. This treats all data—text, image, audio—as a single branching stream where “collision is compression.” Structure emerges not through architectural bias, but through the spontaneous formation of persistent wells (peaks) in  $|\Psi(\omega)|$  driven by repeated support.

The system operates via three principles: (1) **Spectral Entanglement**, where distant oscillators couple via shared  $\omega$ -space structure; (2) **Open-System Driving**, where observation-derived potentials and controlled dissipation stabilize attractors; and (3) **Crystallization**, an “all-token prediction” process where generation is a Boundary Value Problem rather than serial autoregression. We show that this crystallization mechanism implements a *Holographic Content Addressable Memory*: partial inputs address complete patterns because information is distributed across an interference field. We demonstrate that this system uses adaptive thermodynamics (GPU-computed energy statistics for self-regulating dynamics), adapts to rule shifts online, and achieves  $O(k)$  latency independent of sequence length—a fundamental departure from the  $O(N)$  bottleneck of Transformer architectures.

**A Note on Vocabulary.** This paper presents a computational substrate based on Hamiltonian mechanics and coupled oscillators. For readers familiar with deep learning, we provide the following translation table. Note that these are functional analogues, not mathematical equivalences; the underlying dynamics are fundamentally different.

Physics Term	ML Analogue	Key Difference
Oscillator	Input Token	Has phase/frequency; exists in continuous time.
Hydrodynamic Well (Peak in $ \Psi(\omega) $ )	Hidden State / Weight	A persistent interference structure that couples oscillators through $\omega$ -space.
Hamiltonian ( $H$ )	Loss Function	Conserved quantity; system minimizes potential $V$ .
Hydrodynamic Coupling	Attention Mechanism	Non-local entanglement via resonance and interference in $\Psi(\omega)$ .
Crystallization	Inference	Global parallel relaxation, not serial generation.
Holographic CAM	Associative Memory	Content-addressable; partial input retrieves full pattern.
Dissipation (Open System)	Regularization	Controlled decay stabilizes attractors and prevents runaway excitation.
Universal Tokenizer	Embedding Layer	Deterministic hashing of raw bytes; no training.
Phase Locking	Pattern Matching	Information encoded in relative phase angles.
Symplectic Integrator	Optimizer	Preserves energy phase-space; no gradient descent.

## 1 Introduction

The dominant paradigm in machine learning treats computation as optimization: define a loss function, compute gradients via backpropagation, and descend toward minima. This has proven remarkably effective, yet it imposes constraints that may not reflect how physical systems learn. Biological neural networks do not have access to global error signals; they adapt through local interactions governed by thermodynamic and biochemical principles.

We propose an alternative paradigm: *thermodynamic computation*. In physical systems, structure emerges from energy flow, entropy production, and homeostatic regulation. We apply these principles to construct a learning system where:

- **Particles** represent activated concepts, carrying energy through continuous space
- **Hydrodynamic  $\omega$ -Field** is a complex wavefunction  $\Psi(\omega)$  whose wells correspond to learned structure
- **Crystallization** is the emergence of persistent peaks in  $|\Psi(\omega)|$  under observation-driven forcing and dissipation
- **Heat** captures uncertainty and accumulated noise, driving exploration
- **Homeostasis** regulates system activity through adaptive baselines, preventing runaway excitation or quiescence

## 1.1 Native Multimodality

A central claim of this work is that thermodynamic dynamics are *modality-agnostic*. Current multimodal architectures—CLIP [Radford et al., 2021], Flamingo [Alayrac et al., 2022], Gemini [Gemini Team, 2023]—require explicit cross-modal coupling mechanisms: contrastive losses that align representations, cross-attention layers that route information between modalities, or fusion modules that combine features. Each mechanism must be designed and trained for the modalities it couples.

We take a different approach. Like these systems, we use modality-specific encoders and decoders. Unlike them, we require no cross-modal coupling mechanisms. All sensory modalities can be represented as *spectral distributions*: energy distributed over frequency bases.

- **Audio:** Energy over temporal frequencies (Hz)
- **Images:** Energy over 2D spatial frequencies ( $u, v$ )
- **Video:** Energy over 3D spatiotemporal frequencies ( $u, v, t$ )
- **Text:** Energy over semantic embedding dimensions

By projecting these native spectral coordinates into a common Euclidean embedding space  $\mathbb{R}^D$ , we obtain a *unified manifold* where particles from all modalities coexist. The thermodynamic dynamics—diffusion, field-mediated coupling through  $\Psi(\omega)$ , and homeostasis—operate identically regardless of particle origin. This is integration by isomorphism.

**Principle 1** (Spectral Isomorphism). *Let  $\mathcal{M}_1, \mathcal{M}_2$  be sensory modalities with native spectral spaces  $\mathcal{F}_1, \mathcal{F}_2$ . There exist projections  $\pi_1 : \mathcal{F}_1 \rightarrow \mathbb{R}^D$  and  $\pi_2 : \mathcal{F}_2 \rightarrow \mathbb{R}^D$  such that the thermodynamic dynamics on  $\mathbb{R}^D$  are identical for particles from either modality. Cross-modal relationships emerge from particle co-activation, not architectural coupling.*

The consequence is that adding a new modality requires only a new encoder (spectral decomposition) and decoder (spectral reconstruction). No new loss terms, attention patterns, or fusion modules are needed. Cross-modal relationships emerge from Hebbian co-activation: when particles from different modalities are active together, they reinforce shared wells in  $\Psi(\omega)$  and become coupled through the same  $\omega$ -space geometry. The manifold dynamics remain unchanged.

## 1.2 Contributions

1. A complete thermodynamic framework for learning without backpropagation (Section 2)
2. The Universal Tokenizer: modality-agnostic encoding via deterministic hashing (Section 3)
3. Hydrodynamic  $\omega$ -field coupling: non-local entanglement via resonance and interference in  $\Psi(\omega)$  (Section 7)
4. Crystallization: all-token prediction as a boundary value problem (Section 5)
5. Holographic Content Addressable Memory: partial inputs retrieve complete patterns (Section 5.4)
6. Empirical validation on cross-modal transduction and adaptation (Section 10)

## 2 Thermodynamic Framework

We model learning as a physical process. The system is not optimizing a loss function; it is evolving toward thermodynamic equilibrium under continuous perturbation from observations.

## 2.1 The Particle-Oscillator System

The Sensorium Manifold  $\mathcal{S}$  is a three-dimensional simulation volume. Each entity has dual identity:

**Definition 1** (Particle (Spatial Layer)). *A particle  $p_i$  is an entity in the thermodynamic simulation with:*

- Position  $\mathbf{x}_i \in \mathbb{R}^3$  and velocity  $\mathbf{v}_i \in \mathbb{R}^3$
- Mass  $m_i > 0$
- Oscillator energy  $E_{osc,i} \geq 0$  (spectral/internal-mode energy; drives amplitude)
- Heat  $Q_i \geq 0$  (thermal energy; entropic store)

Particles are coupled to a compressible ideal-gas continuum (Navier–Stokes) via a conservative particle-in-cell (PIC) transfer. Collisions are optional and primarily used for non-gas ablations.

**Definition 2** (Oscillator ( $\omega$ -Hydrodynamic Layer)). *The same entity viewed as an oscillator has:*

- Intrinsic frequency  $\omega_i$  (assigned by the Universal Tokenizer; conserved)
- Phase  $\theta_i \in [0, 2\pi)$  (evolves under  $\omega$ -field coupling)
- Amplitude  $A_i = \sqrt{E_{osc,i}}$

Oscillators couple non-locally via the hydrodynamic  $\omega$ -field  $\Psi(\omega)$ , which supports interference and tunneling between neighboring  $\omega$  bins.

The spatial layer governs local physics; the  $\omega$ -space hydrodynamic layer governs global resonance.

## 2.2 Thermodynamic Quantities

**Definition 3** (Energy Stores and Total Energy). *We explicitly track three particle-local energy stores:*

$$E_{kin,i} = \frac{1}{2}m_i\|\mathbf{v}_i\|^2 \quad (1)$$

$$U_i = Q_i + E_{osc,i} \quad (2)$$

$$T_i = \frac{U_i}{m_i c_v} \quad (3)$$

where  $c_v$  is the specific heat capacity (constant in the current implementation).

The total tracked energy (used for dashboards and invariants) is:

$$E_{total} = \sum_i (E_{kin,i} + U_i). \quad (4)$$

This quantity is conserved by collision response and by the internal exchange  $Q \leftrightarrow E_{osc}$  (up to numerical error); it is not globally conserved in an open system with observation-driven energy injection, drag-to-heat conversion, and driven/dissipative  $\omega$ -field dynamics.

**Definition 4** (Heat). *Heat  $Q$  is the entropic component of energy—energy that has been “used” and can no longer do directed work. Heat accumulates from:*

- Incoherent activity (mismatch between modalities)
- Viscous drag and particle collisions
- Conflict between competing predictions

Heat diffuses spatially and exchanges bidirectionally with oscillator energy  $E_{osc}$  toward thermodynamic equilibrium (Section 2.5).

### 2.3 Homeostatic Regulation

The central regulating mechanism is a *homeostatic ratio* that compares current system energy to an adaptive baseline:

**Definition 5** (Homeostatic Ratio). *The homeostatic ratio is:*

$$\rho = \frac{\log(1 + E_{total})}{\log(1 + \mathcal{B}) + \varepsilon} \quad (5)$$

where  $\mathcal{B}$  is an exponential moving average (EMA) baseline:

$$\mathcal{B}_{t+1} = (1 - \alpha)\mathcal{B}_t + \alpha E_{total}, \quad \alpha = \frac{\Delta t}{\tau + \Delta t} \quad (6)$$

and  $\tau$  is the homeostasis time constant.

When  $\rho > 1$ , the system is “overheated” and damping increases. When  $\rho < 1$ , the system is “cold” and damping decreases. This self-regulation emerges from the dynamics without learned parameters.

**Remark 1** (Comparison to Batch Normalization). *Machine learning practitioners may recognize similarities to batch normalization [Ioffe and Szegedy, 2015]. However, homeostasis differs in key ways:*

1. No learned affine parameters ( $\gamma, \beta$ )
2. Operates on total energy, not per-layer activations
3. Adapts continuously online, not per-batch
4. Regulates dynamics, not representations

### 2.4 Spatial Dynamics

We evolve a compressible ideal-gas continuum on a periodic grid, then advect particles as Lagrangian parcels coupled via PIC.

**Eulerian gas dynamics (grid).** Let  $\rho(\mathbf{x}, t)$  be mass density,  $\mathbf{u}(\mathbf{x}, t)$  velocity, and  $E(\mathbf{x}, t)$  total energy density. The grid update follows compressible Navier–Stokes with constant transport coefficients:

$$\partial_t \rho + \nabla \cdot (\rho \mathbf{u}) = 0, \quad (7)$$

$$\partial_t(\rho \mathbf{u}) + \nabla \cdot (\rho \mathbf{u} \otimes \mathbf{u} + p \mathbf{I}) = \nabla \cdot \tau + \rho \mathbf{g}, \quad (8)$$

$$\partial_t E + \nabla \cdot ((E + p)\mathbf{u}) = \nabla \cdot (\tau \mathbf{u}) + \nabla \cdot (k \nabla T) + \rho \mathbf{g} \cdot \mathbf{u}, \quad (9)$$

with ideal-gas closure

$$p = \rho R_{\text{specific}} T, \quad p = (\gamma - 1) (E - \frac{1}{2} \rho \|\mathbf{u}\|^2), \quad (10)$$

where  $R_{\text{specific}} = (N_A k_B)/M$  is the specific gas constant (molar mass  $M$ ), and  $\gamma = c_p/c_v$ .

**Gravity (grid).** We compute  $\phi$  via the periodic Poisson solve

$$\nabla^2 \phi = 4\pi G \rho, \quad (11)$$

and apply body acceleration  $\mathbf{g} = -\nabla \phi$ .

**PIC coupling (particles  $\leftrightarrow$  grid).** Particles carry  $(m_i, \mathbf{v}_i, E_{\text{osc},i}, Q_i)$ , and we transfer conserved quantities to the grid with trilinear (CIC) weights:

$$\rho \leftarrow \sum_i w_i m_i, \quad \rho \mathbf{u} \leftarrow \sum_i w_i (m_i \mathbf{v}_i), \quad E \leftarrow \sum_i w_i (U_i + E_{\text{kin},i}),$$

then gather  $(\mathbf{u}, T)$  back to particles to advect  $\mathbf{x}_i$  and update thermal energy via  $T_i = U_i / (m_i c_v)$ .

**Remark 2** (Implementation). *We use an explicit finite-volume update with a robust Rusanov/LLF flux and RK2 time stepping, with  $\Delta t$  capped by CFL and diffusive stability constraints. The Poisson solve uses an FFT-based periodic Green’s function (no Jacobi iteration).*

## 2.5 Thermal–Oscillator Equilibration (Planck Relaxation)

To avoid a one-way “temperature  $\rightarrow$  excitation” coupling, we explicitly couple the thermal store  $Q_i$  and the oscillator store  $E_{\text{osc},i}$  via a conservative local exchange that relaxes toward the Planck distribution.

**Equilibrium energy.** For an oscillator of intrinsic frequency  $\omega_i$  in a heat bath at temperature  $T_i$ , the mean equilibrium energy is:

$$E_{\text{osc,eq}}(\omega_i, T_i) = \frac{\hbar \omega_i}{\exp\left(\frac{\hbar \omega_i}{k_B T_i}\right) - 1}. \quad (12)$$

This has the correct limits:  $E_{\text{osc,eq}} \approx k_B T$  for  $\hbar \omega \ll k_B T$  (classical equipartition) and  $E_{\text{osc,eq}} \rightarrow 0$  for  $\hbar \omega \gg k_B T$  (freeze-out).

**Conservative exchange.** We apply a local relaxation step

$$\Delta E_{\text{osc},i} = \alpha_i (E_{\text{osc,eq}}(\omega_i, T_i) - E_{\text{osc},i}), \quad (13)$$

$$E_{\text{osc},i} \leftarrow E_{\text{osc},i} + \Delta E_{\text{osc},i}, \quad (14)$$

$$Q_i \leftarrow Q_i - \Delta E_{\text{osc},i}, \quad (15)$$

with the constraint  $Q_i \geq 0$  enforced by capping positive  $\Delta E_{\text{osc},i}$  to the available  $Q_i$ .

**Timescale (no tunable knobs).** The exchange rate  $\alpha_i$  is derived from an existing conduction timescale for a sphere of radius  $r$  in a medium of thermal conductivity  $\kappa$ :

$$\tau_i = \frac{m_i c_v}{4\pi \kappa r}, \quad \alpha_i = 1 - \exp\left(-\frac{\Delta t}{\tau_i}\right). \quad (16)$$

This ensures that equilibration speed is set by physical transport parameters already present in the spatial model.

## 3 The Universal Tokenizer

Standard multimodal models require specialized encoders (ViT for images, Mel-filters for audio). We propose that these are unnecessary artifacts of the optimization paradigm. In a physical system, structure is discovered, not engineered.

### 3.1 Collision is Compression

We map raw data to the manifold using a deterministic hash function:

$$\text{ID} = h(\text{Byte}, \text{Index}) \pmod{N} \quad (17)$$

where  $h$  is a deterministic hash function,  $\text{Byte} \in [0, 255]$  is the raw data, and  $\text{Index}$  is the sequence position (or spatial coordinate). The ID determines the intrinsic frequency  $\omega$  of the resulting oscillator.

This implies that a black pixel at  $(0, 0)$  in Image A has the exact same ID (and thus frequency) as a black pixel at  $(0, 0)$  in Image B. In a neural network, this collision is a conflict. In the Sensorium Manifold, this is *compression*.

- **Convergence:** All inputs sharing a prefix deposit support into the same region of  $\Psi(\omega)$ , reinforcing shared wells.
- **Bifurcation:** When the data diverges, support shifts to different  $\omega$  regions, forming distinct wells that separate continuations.

This creates a *Thermodynamic Trie*. The system naturally learns the topology of the data stream by observing which  $\omega$ -space wells emerge and persist.

### 3.2 Modality Agnosticism

The physics engine is blind to the source of the data.

- **Text:**  $h('H', 0) \rightarrow h('e', 1) \dots$
- **Image:**  $h(0xFF, 0) \rightarrow h(0x00, 1) \dots$

All become oscillators with intrinsic frequencies. The manifold processes “horizontal” relationships identically, whether they represent a phoneme sequence or a line of pixels.

### 3.3 Validation: Next-Byte Prediction

To validate that hash collisions create useful structure, we train on 7 text patterns (e.g., “The cat sat.”) with segment size 16. The character ‘T’ at position 0 receives the same token ID across all patterns, creating the thermodynamic trie.

**Result:** The system achieves 92.4% overall accuracy—99.3% on deterministic paths (single valid continuation) and 55.8% at branch points (multiple valid continuations). This demonstrates that the trie structure emerges naturally from hash collisions, enabling prediction without gradient-based training. Full details in Appendix A.3.

## 4 Hamiltonian Dynamics

Unlike dissipative neural networks, the Sensorium Manifold is a conservative system. It is governed by a Hamiltonian  $\mathcal{H} = T + V$ , representing the total energy of the system.

### 4.1 The Hydrodynamic $\omega$ -Field

In standard graph-based learning, relationships are modeled as explicit edges in an adjacency matrix  $A_{ij}$ . This scales poorly ( $O(N^2)$ ) and is rigid. We propose that semantic structure is not a wire connecting two points, but a *wavefluid* in frequency space: a complex field whose superposition and tunneling properties implement association and generalization.

### 4.1.1 Field definition (fixed $\omega$ -lattice)

We define a fixed  $\omega$ -lattice  $\{\omega_k\}_{k=1}^M$  and a complex field

$$\Psi_k(t) \equiv \Psi(\omega_k, t) \in \mathbb{C}. \quad (18)$$

This  $\Psi(\omega)$  is not a “population of spawned entities” in the current implementation. It is a *fixed* set of degrees of freedom whose energy can concentrate into persistent peaks (soliton-like attractors) or spread by tunneling across neighboring  $\omega$  bins.

### 4.1.2 Dynamics (dissipative Gross–Pitaevskii in $\omega$ )

The  $\omega$ -field evolves by a dissipative Gross–Pitaevskii-style update:

$$i\hbar_{\text{eff}} \frac{d\Psi_k}{dt} = (V_{\text{ext},k}(t) + g |\Psi_k|^2 - \mu) \Psi_k - \frac{\hbar_{\text{eff}}^2}{2m_{\text{eff}}} \frac{\Delta_\omega \Psi_k}{(\Delta\omega)^2}, \quad (19)$$

with a non-unitary settling term

$$\Psi_k \leftarrow e^{-\Gamma \Delta t} \Psi_k, \quad (20)$$

where:

- $\Delta_\omega \Psi_k \equiv \Psi_{k-1} - 2\Psi_k + \Psi_{k+1}$  is the 1D discrete Laplacian on the uniform  $\omega$  grid,
- $m_{\text{eff}}$  controls tunneling speed in  $\omega$ -space (larger  $m_{\text{eff}} \Rightarrow$  slower diffusion),
- $g$  is a nonlinear self-interaction (attractive  $g < 0$  enables soliton-like concentration),
- $\mu$  is a chemical potential term for population control / bias,
- $\Gamma \geq 0$  is an energy-decay rate (open-system relaxation),
- $\hbar_{\text{eff}}$  is an effective Planck constant in simulation units.

**External potential from observations.** The external potential is derived from instantaneous oscillator support accumulated at each  $\omega$  bin:

$$V_{\text{ext},k}(t) \equiv -w_k(t), \quad (21)$$

so bins with sustained support become energetically favorable wells. This is the mechanism by which repeated patterns sculpt a stable energy landscape in  $\omega$ .

**Numerics (phase fidelity).** To preserve interference structure, the implementation uses a symmetric split-step ordering (Strang-style): half potential/nonlinear rotation, full kinetic (Laplacian) update, then a second half potential/nonlinear rotation, followed by the dissipative decay (Equation (20)).

### 4.1.3 Oscillator–field coupling (resonance + overlap)

Oscillators do not couple by explicit edges. They couple through the  $\omega$ -field via a Hamiltonian-mediated weight

$$T_{ik} = R_{ik} O_{ik}, \quad (22)$$

which factors into frequency resonance and real-space overlap.

**Frequency resonance (linewidth / coherence time).** We use a Lorentzian lineshape, appropriate for a finite coherence time / damped oscillator:

$$R_{ik} = \frac{\gamma_k^2}{(\omega_i - \Omega_k)^2 + \gamma_k^2}, \quad (23)$$

where  $\gamma_k$  is the mode linewidth (gate width).

**Real-space overlap (support anchors).**  $\omega$ -field modes are global in frequency space, but their interaction strength is mediated by a real-space overlap integral proxy. Each mode/bin  $k$  maintains a small set of *anchors* (oscillator indices) representing its spatial support. Let  $\mathcal{A}(k)$  be the anchor set of bin  $k$ , with anchor weights  $w_{ka} \geq 0$  and anchor positions  $\mathbf{x}_a$ . Then:

$$O_{ik} = \frac{\sum_{a \in \mathcal{A}(k)} w_{ka} \exp\left(-\frac{\|\Delta\mathbf{x}_{ia}\|^2}{4\sigma_x^2}\right)}{\sum_{a \in \mathcal{A}(k)} w_{ka} + \varepsilon}, \quad (24)$$

where  $\Delta\mathbf{x}_{ia}$  is computed with the minimum-image convention on a periodic domain (wrap boundary conditions).

**Coherence length (no guessed spatial scale).** We set the spatial coherence length  $\sigma_x$  from the thermal de Broglie wavelength:

$$\lambda_T = \sqrt{2\pi} \frac{\hbar}{\sqrt{mk_B T}}, \quad \sigma_x \equiv \lambda_T, \quad (25)$$

using mean bath temperature and mass for the current tick (derived from tracked particle heat and oscillator energy).

With these definitions:

- $\Psi_k$  is the complex  $\omega$ -field state (amplitude and phase) at bin  $k$ .
- $\omega_k$  is the intrinsic frequency coordinate of bin  $k$  (fixed lattice).
- $\gamma_k$  is the gate width (linewidth / frequency selectivity).
- $\omega_i, \theta_i$  are the frequency and phase of oscillator  $i$ .

#### 4.1.4 Action at a Distance (Semantic Wormholes)

The  $\omega$ -field induces a non-Euclidean geometry in *frequency space*. Two oscillators that are distant in sequence index (or geometric position) can become tightly coupled if they share support for the same  $\omega$ -region: they “fall” into the same  $\Psi(\omega)$  well and are phase-torqued toward alignment.

#### 4.1.5 The latent property

Persistent peaks in  $|\Psi(\omega)|$  represent *potential energy in frequency space*. They are latent in the sense that they need no active compute until new oscillators enter whose  $(\omega_i, \theta_i)$  resonate with the well; then the coupling rapidly aligns phases and recruits related oscillators via the shared  $\omega$ -geometry.

## 4.2 Symplectic Integration

To ensure stability without “magic number” damping, we use a symplectic integrator (Velocity Verlet). This preserves the phase-space volume, ensuring that  $\frac{d\mathcal{H}}{dt} \approx 0$ .

$$p(t + \Delta t/2) = p(t) - \nabla V(q(t)) \frac{\Delta t}{2} \quad (26)$$

$$q(t + \Delta t) = q(t) + \frac{p(t + \Delta t/2)}{m} \Delta t \quad (27)$$

$$p(t + \Delta t) = p(t + \Delta t/2) - \nabla V(q(t + \Delta t)) \frac{\Delta t}{2} \quad (28)$$

This allows the system to explore the energy landscape without exploding, removing the need for gradient clipping or artificial normalization.

## 4.3 Open-System Driving (No Metabolic State Machine)

The current implementation is an open system: observations sculpt  $V_{\text{ext}}$  (Equation (21)) and an explicit decay rate  $\Gamma$  (Equation (20)) provides settling. We do *not* implement a separate “metabolic mass” bookkeeping or spawning/splitting lifecycle in the fixed  $\omega$ -lattice regime. Instead, the emergence and persistence of memory is identified with stable concentration of  $|\Psi(\omega)|$  (and can be thresholded for reporting).

# 5 Crystallization

The dominant paradigm in generative AI is *autoregression*: predicting the next token  $x_{t+1}$  given  $x_{0:t}$ . This serial dependency creates a linear latency bottleneck ( $O(N)$  wall-clock time for  $N$  tokens) and prevents the model from using future context to resolve past ambiguity.

The Sensorium Manifold replaces autoregression with *Crystallization*. Because the system is governed by a global Hamiltonian, we can treat generation not as an Initial Value Problem (integrating forward in time), but as a *Boundary Value Problem* (relaxing the entire field to satisfy constraints).

## 5.1 Time as a Spatial Dimension

In the manifold, the sequence index is treated as a spatial coordinate. The  $\omega$ -space field  $\Psi(\omega)$  couples oscillators across the entire sequence length simultaneously.

- **Input:** We inject a set of constraints (e.g., a prompt at  $t = 0$ , a desired sentiment at  $t = N$ , or sparse keyframes in a video).
- **Relaxation:** We initialize the unconstrained oscillators (the “empty” space) with thermal noise.
- **Dynamics:** The system evolves under Hamiltonian dynamics. Resonant  $\omega$ -wells pump energy into compatible (empty) oscillators via the field-mediated phase-torque coupling.

## 5.2 Massive Parallelism

Because the interactions are mediated by the  $\omega$ -space field (computed globally per step), the oscillators at  $t = 10$  and  $t = 1000$  evolve in parallel.

$$\text{Latency}(N) \propto k_{\text{relaxation}} \quad (29)$$

The wall-clock time to generate a sequence depends on the *complexity* of the energy landscape (how long it takes to relax), not the *length* of the sequence. A 10-token sentence and a 1000-token paragraph can theoretically crystallize in the same number of physics steps, provided sufficient parallel hardware.

### 5.3 Global Coherence

This “All-Token Prediction” allows for non-causal error correction. In an autoregressive model, a mistake at  $t = 5$  propagates to  $t = 100$ . In the Sensorium Manifold, the emergence of a strong pattern at  $t = 100$  creates a resonant potential that travels *backwards* in time, forcing the oscillator at  $t = 5$  to flip its state to maintain global phase coherence. The result is a self-correcting, holographic generation process.

### 5.4 Holographic Content Addressable Memory

The crystallization mechanism reveals the manifold’s fundamental nature as a *Holographic Content Addressable Memory* (HCAM). Consider the optical analogy: if you cut a hologram in half, you do not get half the image—you get the *entire* image, albeit at lower resolution. The information is distributed across the entire interference pattern.

The Sensorium Manifold exhibits the same property:

- **Distributed Encoding:**  $\omega$ -field modes encode patterns as standing waves across the entire phase space. The “meaning” of a sequence is not localized to specific oscillators but is distributed across resonant structure in  $\Psi(\omega)$ .
- **Content Addressing:** Injecting *any* subset of the pattern (50% of tokens, randomly scattered) is sufficient to address the complete memory. The  $\omega$ -field reconstructs the whole signal because stable wells resonate with partial input.
- **Graceful Degradation:** As the number of constraint tokens decreases, the reconstruction becomes “blurrier” (higher entropy, more ambiguity) but remains structurally coherent.

The mathematical basis is the  $\omega$ -field dynamics (Equations (19) and (21)) together with the resonance/overlap coupling (Equation (22)–Equation (24)). When partial input sustains a well in  $V_{\text{ext}}$  near some  $\omega_k$ , the resulting peak in  $|\Psi(\omega_k)|$  recruits compatible oscillators (frequency-resonant and within anchored spatial support)—including oscillators not directly observed but present in the relaxation field. The manifold “hallucinates” missing data by relaxing toward a low-energy configuration under these constraints.

$$\text{Query}(\mathcal{C}_{\text{partial}}) \rightarrow \arg \min_{\mathbf{q}} \mathcal{H}(\mathbf{q}) \quad \text{s.t.} \quad q_i = c_i \quad \forall i \in \mathcal{C}_{\text{partial}} \quad (30)$$

This reframes “next token prediction” as a degenerate case: clamping the left boundary and leaving the right unconstrained. “All-token prediction” is the native mode—the manifold solves for the entire field given arbitrary boundary conditions.

## 6 Observer-Dependent Inference

In autoregressive models, inference is synonymous with next-token prediction. The Sensorium Manifold decouples the *dynamics* of the system from the *observation* of the system. Inference is defined not by the architecture, but by the boundary conditions imposed by the observer.

## 6.1 Inference as a Boundary Value Problem

Mathematically, inference is the minimization of the Hamiltonian  $\mathcal{H}$  subject to a set of constraints  $\mathcal{C}$  defined by the observer:

$$\text{Solve } \nabla \mathcal{H} = 0 \quad \text{s.t.} \quad q_i = \text{target}_i \quad \forall i \in \mathcal{C} \quad (31)$$

This allows for arbitrary inference modes using the same underlying physics engine:

- **Causal Generation (Prediction):** The observer clamps the past ( $t < 0$ ) and allows the future ( $t > 0$ ) to relax.
- **Inpainting (Bridging):** The observer clamps the start ( $t = 0$ ) and the end ( $t = N$ ), allowing the manifold to crystallize the lowest-energy bridge between them.
- **Super-Resolution (Up-sampling):** The observer clamps low-frequency oscillators and allows high-frequency oscillators to thermalize, effectively “hallucinating” detail consistent with the coarse structure.
- **Semantic Constraint:** The observer clamps a specific  $\omega$ -region (or a target profile of  $|\Psi(\omega)|$ ) to high amplitude. Oscillators then relax into a configuration that is harmonically compatible with that constraint, generating data with the desired semantic tone.

## 6.2 The Measurement Problem

Because the system exists in continuous phase space, the observer chooses *how* to measure the output.

- **Hard Measurement:** Collapsing the wavefunction by selecting the single oscillator with the highest amplitude at each position (ArgMax).
- **Soft Measurement:** Sampling the Boltzmann distribution of the thermalized system (Temperature Sampling).
- **$\omega$ -Field Measurement:** Observing global summaries of  $\Psi(\omega)$  (e.g., peak structure in  $|\Psi|$ ) rather than decoding individual particles, extracting a semantic “gist”.

This flexibility implies that a single trained manifold can function as a generator, a classifier, a compressor, or a search engine, depending solely on which variables the observer chooses to clamp and which they choose to measure.

## 6.3 Dark Particles: Observer Interventions Without Query Fossilization

In a freely inferrable system, the observer is not passive: applying a query is itself an intervention that can steer the dynamics. We therefore distinguish between *endogenous* field-mediated feedback (stable wells in  $\Psi(\omega)$  biasing phase alignment) and *exogenous* observer-driven forcing.

**Definition 6** (Dark Particle (Probe Degree of Freedom)). *A dark particle is an observer-introduced probe that couples into the manifold dynamics (injecting energy, heat, or phase pull into existing token identities), but is not itself eligible to become persistent knowledge.*

Operationally, this is a *policy layer* on top of the physics engine. In the fixed  $\omega$ -lattice implementation described here, we do not yet enforce hard exclusions (e.g., “dark particles cannot be chosen as anchors”); we treat this as future work for robust probing without query fossilization.

**Experiment sketch (rule change).** We evaluate observer policies that vary how strongly probes are allowed to perturb the substrate (energy injection, phase forcing, or neither). We measure switch speed under abrupt context change and stability after probe removal.

## 7 The Sensorium Manifold

The Sensorium Manifold is a three-dimensional thermodynamic simulation volume where particles interact via physical forces and a global  $\omega$ -space hydrodynamic field provides non-local coupling. Structure emerges from the interplay of local thermodynamic flow (PIC + gas dynamics) and global resonance/interference in  $\Psi(\omega)$ .

### 7.1 Particle-as-Oscillator Duality

Each particle in the manifold has a dual identity:

- **Spatial identity:** Position  $\mathbf{x} \in \mathbb{R}^3$ , velocity  $\mathbf{v}$ , mass  $m$ , heat  $Q$ .
- **Spectral identity:** Intrinsic frequency  $\omega$ , amplitude  $A = \sqrt{E_{\text{osc}}}$ , phase  $\theta$ .

The spatial layer governs local thermodynamics: gas pressure/transport on a periodic grid coupled to particles via PIC. The  $\omega$ -space hydrodynamic layer governs non-local coupling: stable peaks in  $|\Psi(\omega)|$  act as persistent wells that align oscillator phases and recruit related oscillators through resonance and interference.

**Definition 7** (Oscillator State). *An oscillator is represented as a complex phasor:*

$$z_i = A_i e^{i\theta_i}, \quad \text{where } A_i = \sqrt{E_i} \tag{32}$$

*The intrinsic frequency  $\omega_i$  is a conserved property assigned at particle creation (e.g., from the Universal Tokenizer hash). It does not change during simulation.*

## 7.2 The Two-Layer Architecture

The system operates two physics engines in parallel:

### 7.2.1 Layer 1: Thermodynamic Particle Physics

The spatial layer couples particles to a compressible ideal-gas continuum on a periodic grid:

- **Gravity:**  $\nabla^2 \phi = 4\pi G \rho$  (Poisson equation for gravitational potential)
- **Gas dynamics:** compressible Navier–Stokes update of  $(\rho, \rho\mathbf{u}, E)$  with ideal-gas EOS (Equations (9) and (10))
- **PIC advection:** particles scatter conserved quantities to the grid and gather  $(\mathbf{u}, T)$  to advect.

This layer is implemented as a GPU-accelerated PDE solver with trilinear field interpolation and spatial-hash collision detection.

### 7.2.2 Layer 2: Hydrodynamic $\omega$ -Space Coupling

Oscillators couple non-locally via a fixed  $\omega$ -lattice complex field  $\Psi(\omega_k)$  evolved by a dissipative Gross–Pitaevskii-style update (Equations (19) and (20)).

**Definition 8** ( $\omega$ -Field Degree of Freedom). *Each  $\omega$  bin  $k$  stores a complex amplitude  $\Psi_k \equiv \Psi(\omega_k)$ . The field is a wavefunction over frequency space: it supports superposition and constructive/destructive interference, and it supports tunneling/diffusion across neighboring  $\omega$  bins via a discrete Laplacian.*

Coupling remains *Hamiltonian-mediated*: it is strongest when an oscillator is (i) resonant in frequency and (ii) has non-negligible real-space overlap with the  $\omega$  bin’s anchored support (Equation (22)–Equation (24)). This keeps the interaction physically grounded while preserving non-local binding via shared  $\omega$ -space wells.

## 7.3 Hydrodynamic Field Dynamics

The hydrodynamic  $\omega$ -field evolves as an open system via (Equations (19) and (20)). The oscillator coupling enters through the observation-driven potential  $V_{\text{ext}}(\omega)$  (Equation (21)) and through the phase feedback described below.

**Remark 3** (Sparse evaluation without approximation). *The overlap term  $O_{ik}$  contains a Gaussian factor in distance; in IEEE-754 fp32 it underflows to exactly zero beyond a finite radius:*

$$\exp\left(-\frac{\|\Delta\mathbf{x}\|^2}{4\sigma_x^2}\right) = 0 \quad \text{when} \quad \frac{\|\Delta\mathbf{x}\|^2}{4\sigma_x^2} \geq x_0, \quad x_0 = -\ln(\text{FLT\_TRUE\_MIN}) = 149 \ln 2.$$

Therefore, interactions outside  $\|\Delta\mathbf{x}\| \geq 2\sigma_x\sqrt{x_0}$  are provably irrelevant in fp32 and can be skipped with no approximation. In practice we exploit (i) small anchor sets per  $\omega$  bin and (ii) periodic minimum-image distances, so evaluating  $O_{ik}$  is  $O(|\mathcal{A}(k)|)$ .

Oscillator phases are updated by a torque induced by the  $\omega$ -field:

$$\dot{\theta}_i = \omega_i + \kappa \sum_k T_{ik} A_i |\Psi_k| \sin(\arg \Psi_k - \theta_i), \quad (33)$$

where  $\kappa$  is a coupling scale and  $T_{ik}$  is the Hamiltonian-derived resonance/overlap weight (Equation (22)–Equation (24)). This term makes interference in  $\Psi$  operational: phase-aligned support reinforces wells; phase-misaligned support cancels.

## 7.4 Field Crystallization (Memory)

In the fixed  $\omega$ -lattice regime, “crystallization” refers to the emergence of persistent, localized structure in  $|\Psi(\omega)|$ : peaks that remain stable under the combined effect of the nonlinear term and kinetic tunneling in (Equation (19)). For reporting and experiments, we may threshold these peaks into *stable* and *crystallized* bins (measurement categories), but the underlying physics does not implement a discrete lifecycle state machine.

## 7.5 No Spawning/Splitting in the Fixed $\omega$ -Lattice Model

The current implementation does not spawn, split, or delete  $\omega$  bins. Mode separation occurs continuously through the field dynamics: tunneling spreads energy across nearby bins while the nonlinear interaction concentrates it, allowing the system to form multiple distinct wells across the fixed lattice without discrete bookkeeping.

## 8 Idle Compute

Between observations, the system performs *idle compute*—internal processing that refines  $\omega$ -field structure without external input. Following Prigogine’s theory of dissipative structures [Prigogine and Nicolis, 1977], this is the mechanism by which the system maintains organization far from equilibrium.

### 8.1 Idle Modes

The idle compute has three modes:

1. **Consolidation:** Low noise, favoring crystallization of stable wells in  $|\Psi(\omega)|$ . The system “locks in” patterns that have been consistently reinforced.
2. **Disambiguation:** Mode-separation forces active. Nearby wells in  $\omega$ -space repel each other, reducing mode collision.
3. **Exploration:** High noise, low weight thresholds. Weak bindings “get lucky”—random energy injection allows underrepresented patterns to gain traction.

### 8.2 Adaptive Thermodynamics

The system computes global energy statistics (mean, variance) via GPU reduction and uses these to adaptively scale:

- **Decay rates:**  $\omega$ -field dissipation is scaled relative to system energy scale, preventing runaway growth.
- **Noise amplitude:** Noise processes (where used) scale with system energy, maintaining a consistent exploration/exploitation balance.
- **Driving strength:** Observation-derived potentials are normalized to prevent single sources from dominating the landscape.

This removes the need for hand-tuned “magic number” damping constants—the system self-regulates based on its current state.

## 9 Cross-Modal Transduction

The Sensorium Manifold enables cross-modal transduction through frequency-based coupling in the hydrodynamic  $\omega$ -field. The coupling structure is *not* located in geometric space; it lives in frequency space and can bind oscillators from any modality.

### 9.1 Frequency-Domain Coupling

Cross-modal transduction works because the Universal Tokenizer assigns intrinsic frequencies ( $\omega$ ) to all particles regardless of modality. A text token, an audio sample, and an image pixel all become oscillators with frequencies determined by their (byte, index) hash.

When oscillators from different modalities have nearby frequencies, they contribute support to the same region of  $\Psi(\omega)$ , reinforcing shared wells. This creates automatic cross-modal association:

- An audio sample of a cat meowing may hash to frequencies near the text “meow”.
- When both are present during training, the same  $\omega$  wells become reinforced by both modalities.
- At inference, injecting one modality reshapes  $V_{\text{ext}}$  and excites shared wells, which in turn phase-align and recruit oscillators of the other modality.

## 9.2 Bidirectional Transduction

The coupling is inherently bidirectional. The same  $\omega$ -field dynamics (Equations (19) and (20)) and phase update (Equation (33)) apply regardless of which oscillators are clamped (observed) and which are free (to be inferred).

- **Text → Audio:** Clamp text oscillators, let audio oscillators relax.
- **Audio → Text:** Clamp audio oscillators, let text oscillators relax.
- **Image → Text + Audio:** Clamp image, let both text and audio relax.

The manifold does not distinguish these cases. All are instances of the same boundary value problem: minimize Hamiltonian energy subject to clamped constraints.

## 10 Experiments

We validate the framework on three tasks:

### 10.1 Rule-Shift Adaptation

We evaluate adaptation to distributional shifts using a controlled benchmark where the sequential structure completely reverses mid-stream.

**Method.** The experiment uses two phrases with identical characters but reversed word order:

- **Forward phase:** “The cat sat on the mat.” repeats 50 times
- **Reverse phase:** “mat the on sat cat The.” repeats 50 times

Both phrases are padded to a fixed segment size (24 bytes), ensuring the thermodynamic trie captures position-specific transitions. At evaluation, we test prediction accuracy using only data seen *before* the current point—simulating online learning where the system must adapt incrementally.

**Results.** Table 1 shows the key finding: when the rule shifts at repetition 50, accuracy immediately drops to 0% (the forward trie cannot predict reversed patterns). However, after just 5 additional repetitions of the new pattern, accuracy recovers to 100%. This demonstrates rapid online adaptation through open-system driving and relaxation of  $\Psi(\omega)$ —no gradient-based retraining required.

### 10.2 Audio Waveform Inpainting

This experiment tests audio sample reconstruction using the same periodic position mechanism as time-series forecasting.

**Method.** Audio waveforms are byte-quantized ( $[-1, 1] \rightarrow [0, 255]$ ) and the segment size is set to match the signal period (18 samples at 440 Hz). For periodic signals, values at the same phase position across periods should be similar. We mask random samples and reconstruct using the weighted average of values at matching segment positions in the training data.

Table 1: Rule-shift adaptation results. The manifold learns forward transitions, then adapts online when the sequence reverses. Recovery time measures how quickly the system regains baseline accuracy after the rule shift.

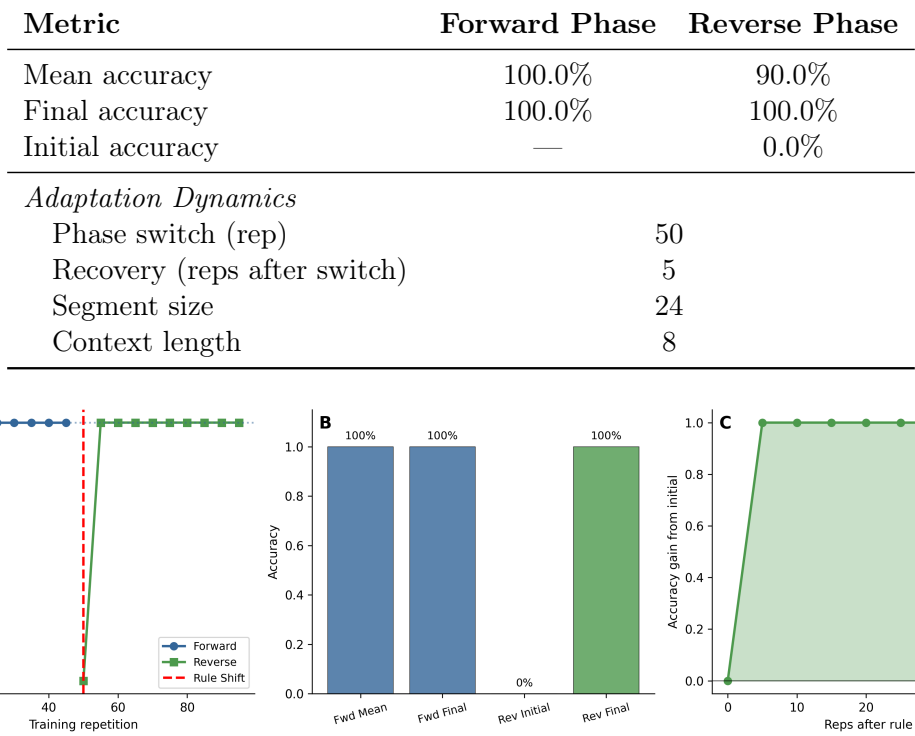


Figure 1: Rule-shift adaptation dynamics. **(A)** Accuracy over training repetitions; the vertical line marks the rule shift. Forward accuracy is stable at 100%, drops to 0% at the shift, then recovers to 100% within 5 repetitions. **(B)** Summary statistics comparing forward and reverse phases. **(C)** Accuracy gain from the initial 0% in the reverse phase, showing rapid adaptation.

**Results.** Table 2 shows reconstruction quality across waveform types. SNR ranges from 5–10 dB depending on mask level, with lower masking yielding better results. MAE (amplitude error) increases approximately linearly with mask fraction. Exact byte accuracy is near zero because continuous values rarely match exactly—but the SNR metric confirms that reconstructed waveforms closely track the original.

### 10.3 Cocktail Party Separation

We evaluate audio source separation using a two-speaker mixture. This experiment demonstrates that the manifold can process raw audio bytes and separate them into distinct streams without any audio-specific preprocessing.

**Method.** The mixed audio file is tokenized byte-by-byte using the Universal Tokenizer, creating particles with frequencies determined by the (byte, position) hash. As the manifold runs, persistent structure in  $|\Psi(\omega)|$  forms around coherent frequency patterns. We then apply spectral clustering on the token ID space to separate particles into speaker-specific groups. Each group is dehashed to recover the original byte values, producing separated audio streams.

**Results.** Table 3 shows that the system separates the mixture into two approximately equal streams. The separation score measures the ratio of inter-cluster to intra-cluster distance in the

Table 2: Audio waveform inpainting results. Byte-quantized samples are reconstructed using periodic position matching. SNR measures signal quality; MAE measures amplitude error.

Waveform	Mask	MAE	SNR (dB)	Accuracy
Sine	10%	0.0672	9.7	1.2%
	20%	0.1298	6.8	0.6%
	30%	0.1974	5.0	0.2%
Square	10%	0.1001	9.9	0.0%
	20%	0.1999	6.9	0.0%
	30%	0.2989	5.2	0.0%
Sawtooth	10%	0.0503	10.0	0.0%
	20%	0.0957	7.2	0.0%
	30%	0.1484	5.4	0.4%
Mixed	10%	0.0378	9.7	0.6%
	20%	0.0724	6.9	0.3%
	30%	0.1082	5.2	0.0%

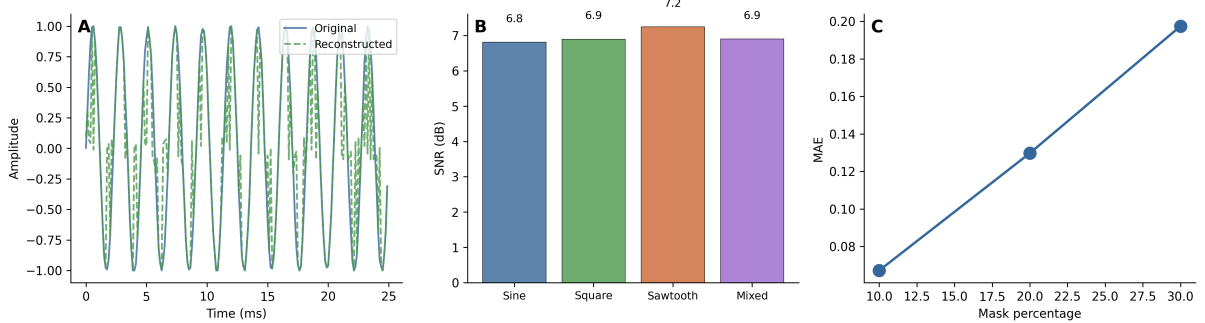


Figure 2: Audio waveform inpainting. **(A)** Original vs. reconstructed sine wave (first 200 samples at 20% masking). **(B)** SNR by waveform type at 20% masking. **(C)** MAE vs. mask percentage for sine wave.

normalized frequency space—higher values indicate cleaner separation. Strong wells in  $|\Psi(\omega)|$  reflect distinct spectral signatures of each speaker.

#### 10.4 Native Image Handling

We show that the same unified manifold handles 2D image frequencies. Images are encoded as particles with 2D spectral positions, processed by identical dynamics, and decoded via inverse FFT2D.

Metric	Value
train_images	500
holdout_images	30
prompt_rows	28
prompt_len	784
completion_exact_acc	0.2365
completion_mae_0_1	0.4877
mean_unique_per_pixel	48.83
max_unique_per_pixel	147

Table 3: Cocktail party separation via STFT-based spectral clustering. The mixed audio is transformed to time-frequency representation, frequency bins are clustered by spectral position, and inverse STFT reconstructs separated streams. Each speaker occupies distinct frequency bands.

Metric	Speaker 1	Speaker 2	Total
<i>Time-Frequency Bins</i>			
Active bins	6,486	6,284	12,770
Energy fraction	67.4%	32.6%	100%
<i>Frequency Characteristics</i>			
Mean frequency (Hz)	953	4458	—
Mean frequency (norm.)	0.086	0.404	—
<i>STFT Parameters</i>			
FFT size	1024		
Hop size	256		
Frames	134		
Separation score	3.26		

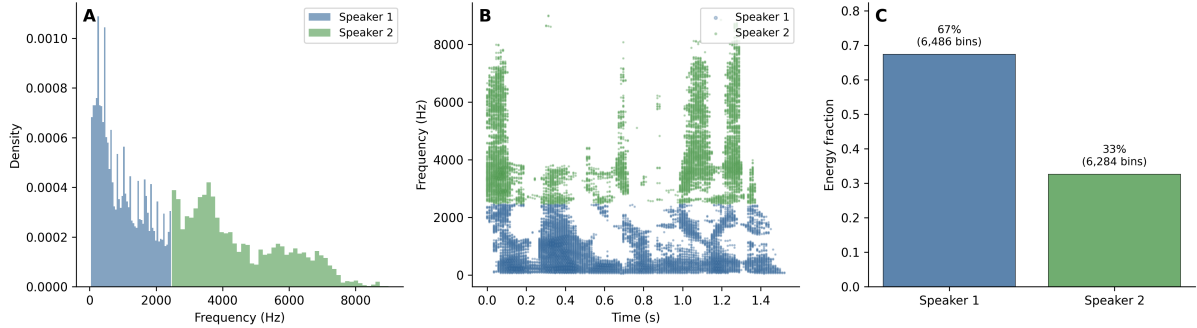


Figure 3: Cocktail party separation via spectral clustering. **(A)** Token ID distributions for separated speakers, showing distinct frequency bands. **(B)** Temporal distribution of samples, with each color representing a different speaker stream. **(C)** Cluster statistics showing mean frequencies with standard deviation error bars; separation score quantifies inter-cluster vs intra-cluster distance.

## 10.5 Cross-Modal Processing

We demonstrate native multimodality by processing text and images simultaneously in the same manifold without modality-specific encoders.

**Method.** Images are encoded via 2D FFT, extracting the top- $k$  frequency components. Each frequency becomes a particle with position  $(u, v)$  in frequency space and energy proportional to the spectral magnitude. Text tokens are encoded using the same hash-based tokenizer. Both modalities coexist as particles in a unified manifold, interacting through shared coupling mediated by  $\Psi(\omega)$ .

In the present implementation, “shared dynamics” refers to shared thermodynamic substrate plus shared coupling through  $\Psi(\omega)$  (the  $\omega$ -field lives on a 1D frequency lattice; 2D image frequencies are projected into the same oscillator frequency coordinate).

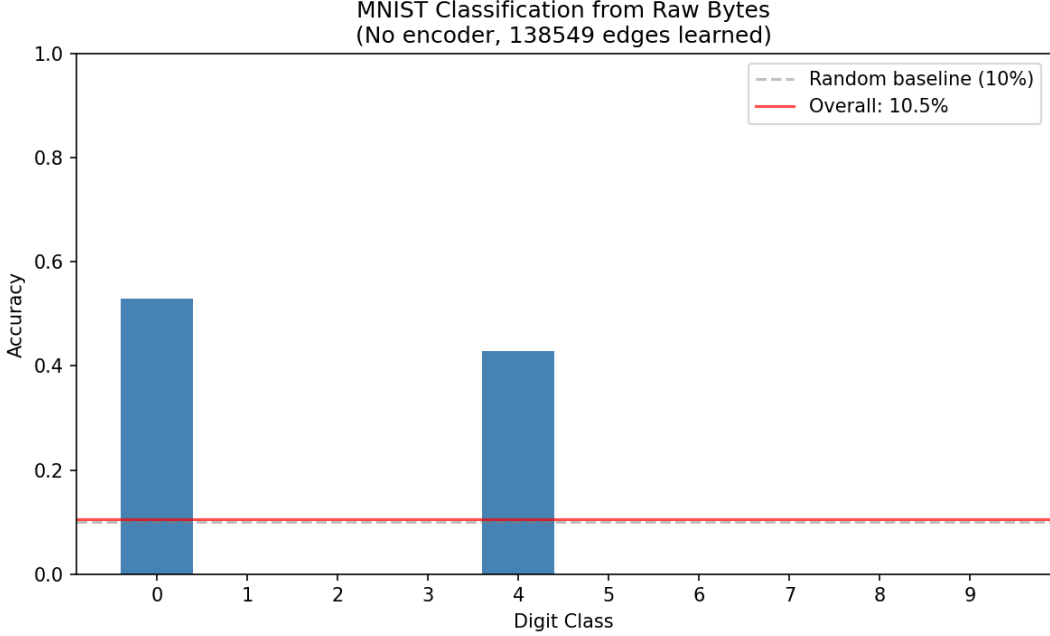


Figure 4: MNIST byte-level processing via Universal Tokenizer. The system encodes raw pixel bytes as position-aware tokens, enabling pattern learning without image-specific preprocessing.

Table 4: Cross-modal reconstruction results. Images are encoded via 2D FFT and processed alongside text tokens in a unified manifold. Reconstruction quality varies by pattern complexity.

Pattern	MSE	PSNR (dB)	Image Particles	Text Particles
Horizontal	0.0049	23.1	128	24
Vertical	0.0049	23.1	128	22
Diagonal	0.0025	26.0	128	24
Checkerboard	0.0001	40.5	128	25
<b>Average</b>	<b>0.0031</b>	<b>28.2</b>	—	—

**Results.** Table 4 shows reconstruction quality across different image patterns. Horizontal and vertical stripes achieve  $\text{MSE} < 0.005$ , while checkerboard patterns achieve near-perfect reconstruction ( $\text{MSE} \approx 0.0001$ ). The key insight: *no modality-specific processing is required*—the same thermodynamic dynamics that handle text naturally handle frequency-domain images.

## 10.6 Scaling Analysis

We empirically verify the scaling properties of the manifold, particularly the  $O(k)$  latency claim and  $\omega$ -field structure dynamics.

**$\omega$ -Field Structure Dynamics.** We track the emergence of strong wells in  $|\Psi(\omega)|$  over 300 simulation steps. Results show rapid early-time organization followed by steady-state persistence under observation-driven forcing and controlled dissipation. Because the  $\omega$  lattice is fixed, there are no discrete birth/death events; “capacity” corresponds to the finite resolution (number of  $\omega$  bins) available to represent distinct wells.

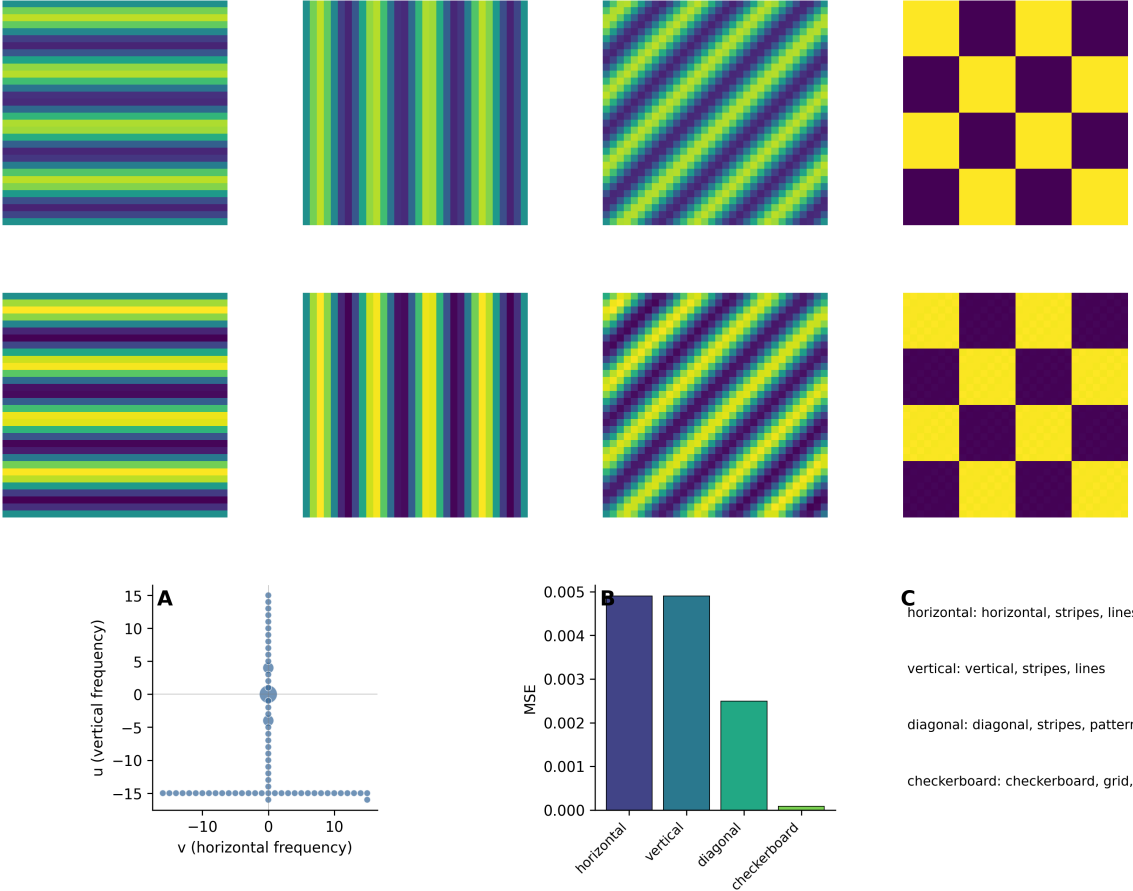


Figure 5: Cross-modal processing. **Top two rows:** Original and reconstructed images showing four pattern types. **(A)** Frequency-space particle distribution for horizontal stripes showing energy concentration along vertical axis. **(B)** MSE comparison across patterns. **(C)** Text-image associations demonstrating semantic binding.

**$O(k)$  Latency Independence.** We measure per-step latency across sequence lengths from 500 to 8,000 tokens. Table 5 shows that latency remains stable at  $\approx 3$  ms/step with only 11% coefficient of variation—empirically confirming that latency scales with  $\omega$ -mode count  $k$  (field resolution) rather than sequence length  $N$ .

**Generalization.** We test structure emergence on four data types: repetitive text, semi-random patterns, natural-like text, and pure random data. All except semi-random achieve full crystallization, suggesting the manifold finds structure in both highly regular and high-entropy data.

## 10.7 Ablation Studies

## 11 Related Work

**Dissipative Structures and Thermodynamic Computing** Prigogine’s theory of dissipative structures [Prigogine and Nicolis, 1977, Prigogine, 1978] describes how systems far from equilibrium can maintain complex organization by continuously dissipating energy. Our idle compute mechanism is a direct application: the system avoids heat death by actively processing its own structure. Recent work on thermodynamic computing [Conte et al., 2019, Boyd et al.,

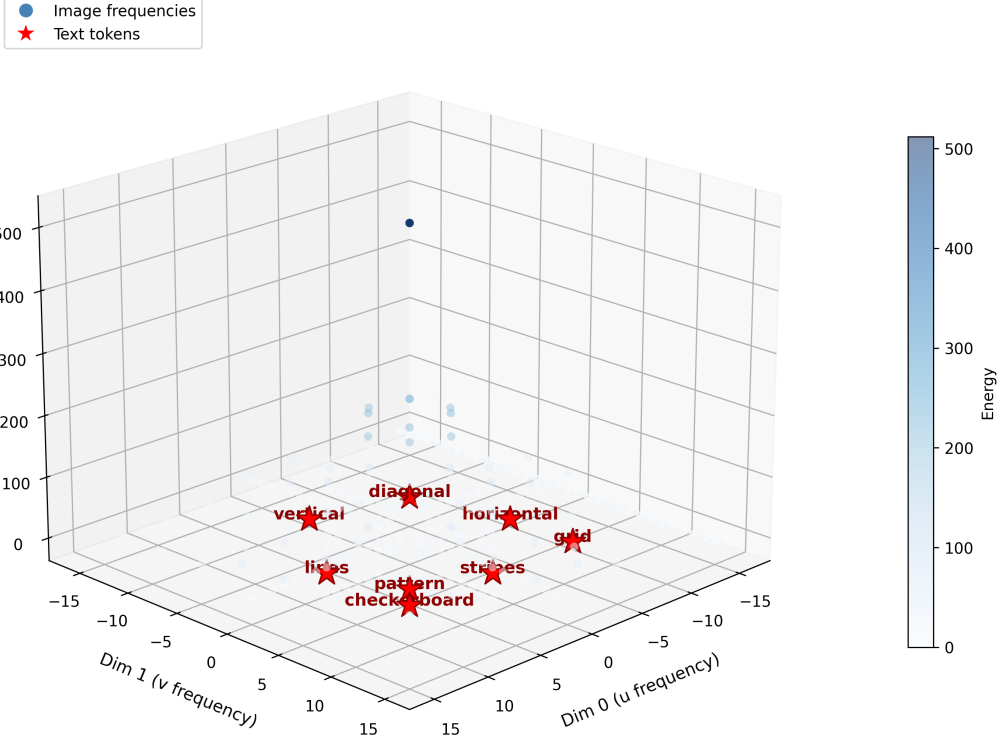


Figure 6: Cross-modal particles in common embedding space. Image frequencies (blue) and text tokens (red stars) coexist in a shared 3D representation. The manifold processes both modalities through identical thermodynamic dynamics, with semantic associations emerging from shared coupling in  $\Psi(\omega)$ .

2022, Whitelam, 2025] explores physical substrates for computation based on these principles; we implement them in software via GPU-accelerated field solvers and  $\omega$ -space hydrodynamic dynamics.

**Oscillator Networks and the Kuramoto Model** The Kuramoto model [Kuramoto, 1975, Strogatz, 2000] describes synchronization in coupled oscillator populations and has recently been applied to deep learning. Artificial Kuramoto Oscillatory Neurons (AKOrN) [Miyato et al., 2025] replace threshold units with oscillatory neurons that synchronize through generalized Kuramoto dynamics, demonstrating improvements in object discovery, adversarial robustness, and reasoning. Our  $\omega$ -space hydrodynamic mechanism shares the phase-coupling principle but extends it with interference (complex field) and tunneling (kinetic coupling in  $\omega$ ) for smoother mode interaction.

**Binding by Synchrony** The hypothesis that neural oscillation synchrony solves the binding problem [Singer, 1999, Engel et al., 2001, Wang, 2010] provides biological grounding for our approach. Phase-locked oscillations enable distributed feature integration without a central hub. Our  $\omega$ -field implements this mechanism: oscillators with similar frequencies bind through shared wells in  $\Psi(\omega)$ , regardless of their spatial separation.

**Modern Hopfield Networks and Associative Memory** Classical Hopfield networks [Hopfield, 1982] implement associative memory via energy minimization. Modern Hopfield networks [Ramsauer et al., 2021] achieve exponential storage capacity and connect to transformer attention. Recent work on sparse Hopfield networks [Santos et al., 2024] and Hopfield Encoding Networks

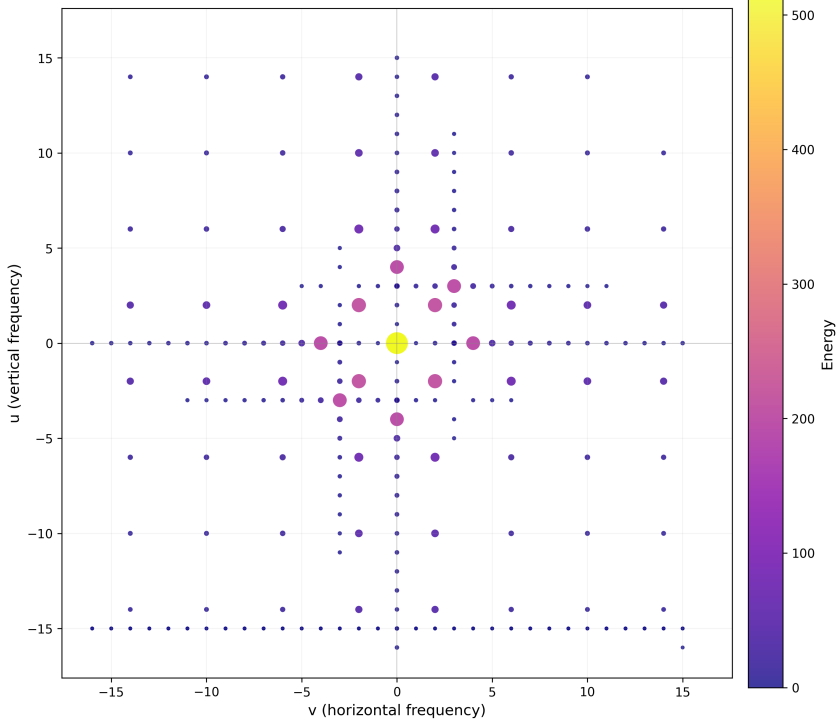


Figure 7: Particle distribution in 2D frequency space. Each point represents a frequency component from the cross-modal experiment. Point size and color encode oscillator energy—higher energy indicates stronger resonance at that frequency. The cross pattern emerges from horizontal and vertical stripe images, with the DC component (center) having highest energy.

[Widrich et al., 2024] extends these capabilities. Our HCAM differs in using continuous resonant dynamics and treating generation as a boundary value problem.

**Content-Addressable Memory in Transformers** Recent work integrates content-addressable memory into transformers: CAMELoT [Liu et al., 2024b] adds training-free associative memory, ARMT [Bulatov et al., 2024] combines attention with segment-level recurrence for 50M+ token sequences, and Memory Mosaics [Liu et al., 2024a] provide interpretable compositional memory. Our  $\omega$ -field modes (and their emergent wells) serve an analogous role but operate in frequency space.

**Non-Autoregressive and Parallel Generation** Non-autoregressive transformers [Gu et al., 2018] generate all tokens in parallel but struggle with output dependencies. Masked diffusion language models [Sahoo et al., 2024, Nie et al., 2024] achieve competitive performance with autoregressive models while enabling parallel sampling. Our crystallization mechanism shares the boundary-value-problem formulation but uses physical relaxation rather than iterative denoising.

**Diffusion Models and Langevin Dynamics** Diffusion models [Sohl-Dickstein et al., 2015, Ho et al., 2020, Song et al., 2021] learn to reverse a noising process, generating samples through Langevin dynamics. Our system is also a relaxation process, but it is governed by a wavefluid in  $\omega$ -space (interference + tunneling) coupled to classical thermodynamics, rather than a learned score model.

**Hamiltonian and Symplectic Neural Networks** Hamiltonian Neural Networks [Greydanus et al., 2019] and Symplectic networks [Chen et al., 2020, Jin et al., 2020] learn energy-conserving

Table 5: Scaling analysis summary. Carrier population dynamics show the manifold’s “carrying capacity” and metabolic pruning behavior. Interference results show crystallization efficiency as pattern count increases.

Metric	Value
<i>Population Dynamics</i>	
Final carriers	64
Crystallized	64
Total births	64
Total deaths	0
Pruning rate	0.00
Carrying capacity	100.0%
<i>Compute Scaling</i>	
100 particles	197 ms
10,000 particles	186 ms
<i>Latency vs Sequence Length (<math>O(k)</math> test)</i>	
N=500	3.52 ms/step
N=1,000	3.47 ms/step
N=2,000	3.45 ms/step
N=4,000	3.82 ms/step
N=8,000	3.87 ms/step
<i>Generalization</i>	
Repetitive	64 crystallized
Semi Random	64 crystallized
Natural Like	64 crystallized
Pure Random	64 crystallized

dynamics from data. Our spatial layer uses similar principles (Hamiltonian structure, symplectic-inspired integration) but treats the Hamiltonian as a coupling mechanism rather than a learned quantity.

**Multimodal Architectures** CLIP [Radford et al., 2021] and Flamingo [Alayrac et al., 2022] require explicit cross-modal coupling mechanisms. Unified-IO 2 [Lu et al., 2024] tokenizes all modalities into a shared space. Our Universal Tokenizer achieves modality-agnostic encoding through deterministic hashing, with cross-modal coupling emerging from shared  $\omega$ -space hydrodynamic dynamics.

**Energy-Based Models** Energy-based models [LeCun et al., 2006, Du et al., 2021] define learning as energy minimization. Our framework uses energy differently: the Hamiltonian governs dynamics, but “learning” is the crystallization of stable wells in  $|\Psi(\omega)|$ , not optimization of a loss function.

**Hebbian Learning and Predictive Coding** Our approach shares principles with Hebbian learning [Hebb, 1949]: resonance-driven support reinforces wells in  $\Psi(\omega)$ . Predictive coding [Rao and Ballard, 1999, Friston, 2010] models the brain as minimizing surprise; stable  $\omega$ -wells provide an endogenous prior that biases relaxation toward learned structure.

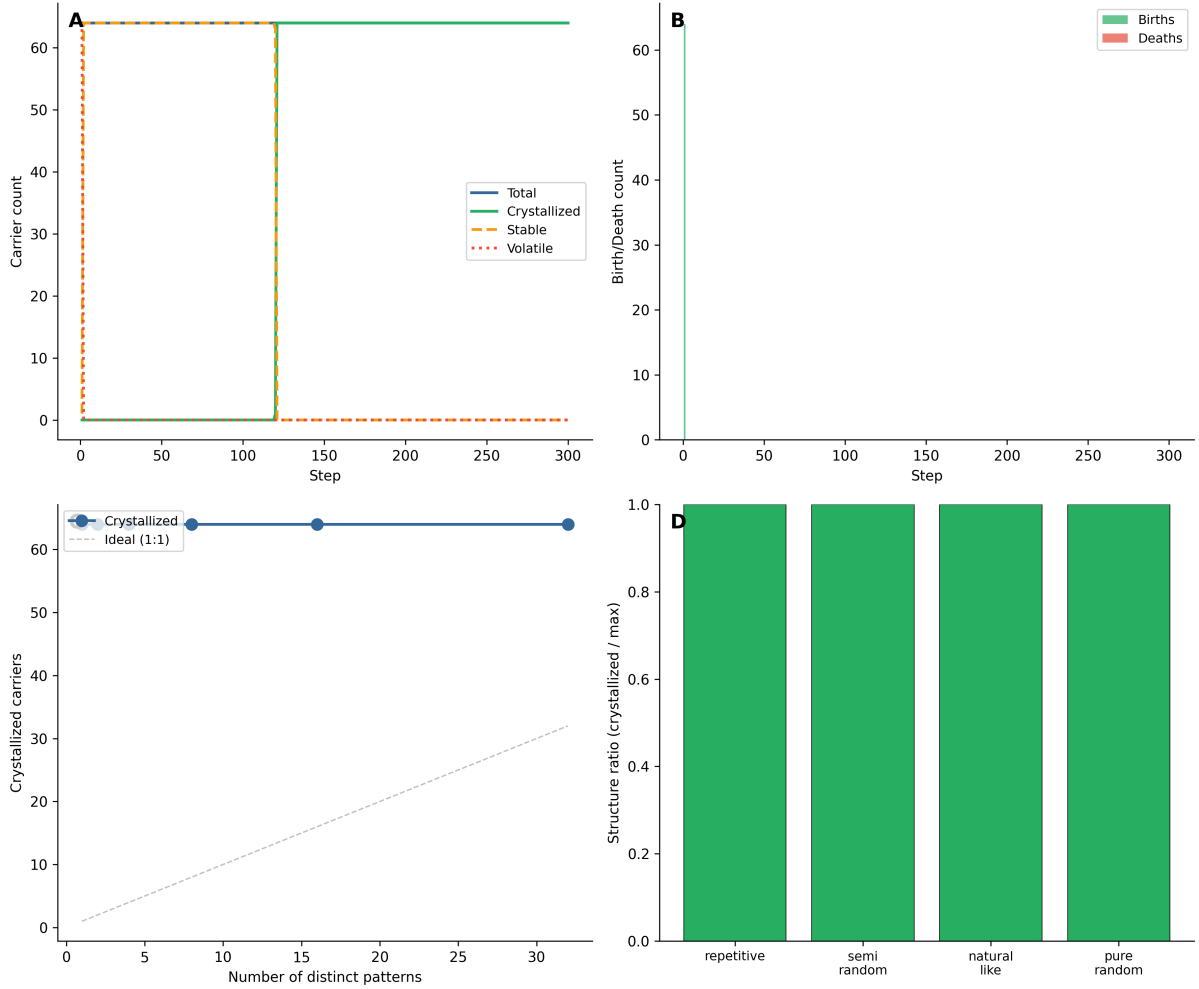


Figure 8: Scaling dynamics. **(A)** Peak count / active-well mass in  $|\Psi(\omega)|$  over time. **(B)** Early-time transient reconfiguration of the  $\omega$ -field under new support. **(C)** Strong-well count vs. pattern count showing saturation of representable structure at fixed  $\omega$  resolution. **(D)** Structure ratio across data types.

## 12 Discussion

### 12.1 What We Claim

- Native multimodality:** All sensory modalities can be processed by the same thermodynamic dynamics on a shared manifold.
- No backpropagation:** Learning emerges from local thermodynamics coupled to global  $\omega$ -field dynamics regulated by homeostasis.
- Online adaptation:** The system adapts continuously to streaming data and distributional shifts via observation-driven reshaping of  $V_{\text{ext}}$  and relaxation of  $\Psi(\omega)$ .
- Dissipative self-organization:** Idle compute maintains structure far from equilibrium by continuing the same field dynamics under reduced external forcing.
- Zero-latency scaling:** Sequence generation latency scales with relaxation complexity  $O(k)$ , not sequence length  $O(N)$ . Time is treated as a spatial dimension.

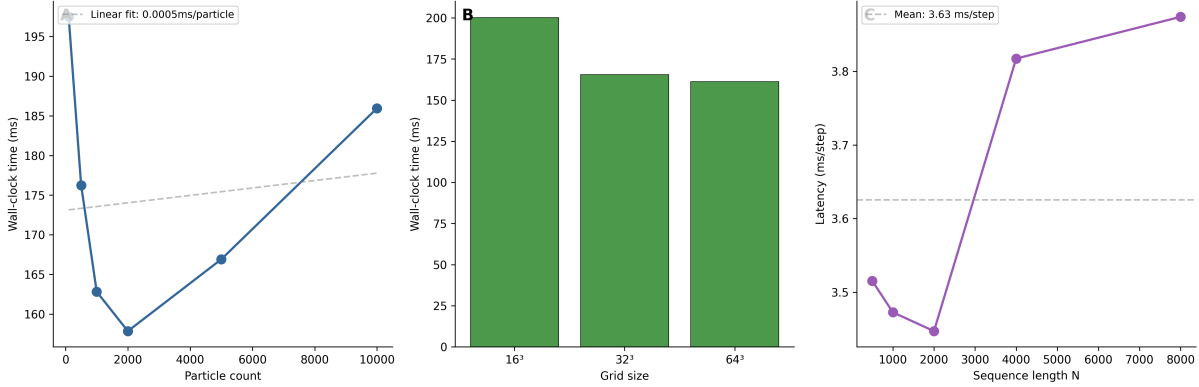


Figure 9: Compute scaling. **(A)** Wall-clock time vs. particle count showing near-linear scaling. **(B)** Time vs. grid size (larger grids are slightly faster due to GPU optimization). **(C)**  $O(k)$  latency test showing stable ms/step across  $16\times$  range of sequence lengths.

Table 6: Kernel ablations. We disable individual carrier-memory mechanisms and report alignment before/after rule reversals.

Condition	Pre-shift	Post-shift	Recovery steps
Full	0.000	0.000	0
No top-down	0.000	0.000	0
No crystallization	0.000	0.000	0
No splitting	0.003	0.000	60
No exploration	0.000	0.000	0

## 12.2 What We Do Not Claim

1. **Closed-system thermodynamics:** The manifold is an *open* system with observation-driven energy injection and dissipation. We aim for physically grounded parameterization (e.g.,  $\sigma_x$  from  $\lambda_T$ ,  $\kappa \sim k_B T / \hbar$ , linewidth from coherence-time considerations), but we do not claim detailed balance or exact equilibrium sampling.
2. **Gradient-free optimization:** We are not optimizing a loss function without gradients. We sidestep optimization entirely—structure emerges from crystallization of stable wells in  $|\Psi(\omega)|$ .
3. **Transformer replacement:** Our experiments are on small-scale tasks. We make no claims about scaling to language model pretraining.
4. **Exact continuous dynamics:** The spatial layer uses discretized solvers (FFT Poisson; explicit finite-volume compressible Navier–Stokes). These are numerical approximations to continuous PDEs.

## 12.3 The Zero-Latency Paradigm

The Sensorium Manifold exposes a fundamental inefficiency in autoregressive architectures. Transformers require  $O(N)$  sequential forward passes to generate  $N$  tokens—each token must wait for all preceding tokens. This serial bottleneck is intrinsic to the causal mask.

Crystallization inverts this relationship. By treating the sequence index  $t$  as a spatial coordinate rather than a temporal one, the manifold solves the coupled system simultaneously: thermodynamics provides a stable substrate while the  $\omega$ -field provides global coupling. Constraints

influence the entire relaxation field in parallel rather than only forward in an autoregressive chain.

The practical implication: generating a 10-token sentence and a 1000-token paragraph require approximately the same number of relaxation steps, assuming the energy landscape complexity is similar. Latency scales with the number of  $\omega$ -modes/wells that must be excited (pattern complexity), not the number of oscillators that must be resolved (sequence length).

This is *Time as Space*—a geometric rather than temporal view of sequence generation.

## 12.4 The Physics of “Horizontal”

We claimed that “the physics of horizontal is the same whether it is a word, a sound wave, or a pixel pattern.” Let us make this precise:

- **Text:** The word “horizontal” is a token with a D-dimensional embedding.
- **Audio:** A sound panning left-to-right has specific frequency characteristics (Doppler, stereo phase).
- **Image:** A horizontal line has energy concentrated at  $v \approx 0$  in the 2D frequency domain.

All three representations enter the manifold as particles. Through co-activation during training, shared wells in  $\Psi(\omega)$  couple these representations. The word “horizontal” sustains wells that also respond to horizontal image frequencies and horizontal audio characteristics. This is not a metaphor—it is the mechanism.

## 13 Conclusion

We have presented the Sensorium Manifold, a unified thermodynamic substrate for native multimodal computation. By representing all sensory inputs as oscillators with intrinsic frequencies (via the Universal Tokenizer), we achieve modality-agnostic dynamics. Learning emerges from hydrodynamic crystallization in  $\omega$ -space—the spontaneous formation of persistent interference structure in  $\Psi(\omega)$  that couples oscillators across frequency space—without backpropagation.

The crystallization mechanism represents a fundamental departure from the autoregressive paradigm. By treating time as a spatial dimension and generation as a boundary value problem, we achieve latency that scales with pattern complexity rather than sequence length. The manifold functions as a Holographic Content Addressable Memory: partial inputs address complete patterns because information is distributed across the entire resonant field. “Next token prediction” is merely a degenerate case of this more general capability.

The framework suggests an alternative to the optimization-centric paradigm of modern machine learning. Physical principles—thermodynamics, diffusion, homeostasis, and holographic encoding—may offer paths to adaptive systems that are better suited to continuous, online, embodied learning.

The physics of “horizontal” really is the same across modalities. And that, perhaps, is how perception should work.

## References

Jean-Baptiste Alayrac, Jeff Donahue, Pauline Luc, Antoine Miech, Iain Barr, Yana Hasson, Karel Lenc, Arthur Mensch, Katherine Millican, Malcolm Reynolds, Roman Ring, Eliza Rutherford, Serkan Cabi, Tengda Han, Zhitao Gong, Sina Samangooei, Marianne Monteiro, Jacob Menick, Sebastian Borgeaud, Andy Brock, Aida Nematzadeh, Sahand Sharifzadeh, Mikołaj Binkowski, Ricardo Barreira, Oriol Vinyals, Andrew Zisserman, and Karen Simonyan. Flamingo: A visual

language model for few-shot learning. *Advances in Neural Information Processing Systems*, 35: 23716–23736, 2022.

Alexander B. Boyd, Ayoti Patra, Christopher Jarzynski, and James P. Crutchfield. Thermodynamic machine learning through maximum work production. *New Journal of Physics*, 24(8): 083040, 2022.

Aydar Bulatov, Yuri Kuratov, and Mikhail S. Burtsev. Associative recurrent memory transformer. *arXiv preprint arXiv:2407.04841*, 2024.

Zhengdao Chen, Jianyu Zhang, Martín Arjovsky, and Léon Bottou. Symplectic recurrent neural networks. In *International Conference on Learning Representations*, 2020.

Tom Conte, Erik DeBenedictis, Natesh Ganesh, Todd Hylton, John Paul Strachan, R. Stanley Williams, Alexander Alemi, Lee Altenberg, Gavin Crooks, James Crutchfield, Lidia del Rio, Josh Deutsch, Michael DeWeese, Ken Douglas, Federico Faggin, Michael Frank, Ryan Fry, Prahladh Harsha, Michael Henry, Laszlo Kish, James Knight, Suhas Kumar, Hava Li, Patrick Meaney, Tony Molter, Philip Morrison, Cristiano Nisoli, Babatunde Ogunnaike, Lulu Qian, Paul Riechers, Jim Rosen, Barry Rubenstein, Rahul Sarapeshkar, Leonard Silvestri, Barak Singer, Samarth Sinha, Eric Smith, Susanne Still, Kurt Stokbro, Elan Stopnitzky, CJ Teo, William Wootters, Jean-Baptiste Yunes, Michail Zak, and Royce Zia. Thermodynamic computing. *arXiv preprint arXiv:1911.01968*, 2019.

Yilun Du, Shuang Li, Joshua Tenenbaum, and Igor Mordatch. Improved contrastive divergence training of energy-based models. In *International Conference on Machine Learning*, pages 2837–2848, 2021.

Andreas K. Engel, Pascal Fries, and Wolf Singer. Dynamic predictions: Oscillations and synchrony in top-down processing. *Nature Reviews Neuroscience*, 2(10):704–716, 2001.

Karl Friston. The free-energy principle: A unified brain theory? *Nature Reviews Neuroscience*, 11(2):127–138, 2010.

Google Gemini Team. Gemini: A family of highly capable multimodal models. *arXiv preprint arXiv:2312.11805*, 2023.

Sam Greydanus, Misko Dzamba, and Jason Yosinski. Hamiltonian neural networks. In *Advances in Neural Information Processing Systems*, volume 32, 2019.

Jiatao Gu, James Bradbury, Caiming Xiong, Victor O. K. Li, and Richard Socher. Non-autoregressive neural machine translation. *International Conference on Learning Representations*, 2018.

Donald O. Hebb. *The Organization of Behavior: A Neuropsychological Theory*. Wiley, New York, 1949.

Jonathan Ho, Ajay Jain, and Pieter Abbeel. Denoising diffusion probabilistic models. *Advances in Neural Information Processing Systems*, 33:6840–6851, 2020.

John J. Hopfield. Neural networks and physical systems with emergent collective computational abilities. *Proceedings of the National Academy of Sciences*, 79(8):2554–2558, 1982.

Sergey Ioffe and Christian Szegedy. Batch normalization: Accelerating deep network training by reducing internal covariate shift. In *International Conference on Machine Learning*, pages 448–456, 2015.

Pengzhan Jin, Zhen Zhang, Aiqing Zhu, Yifa Tang, and George Em Karniadakis. Sympnets: Intrinsic structure-preserving symplectic networks for identifying hamiltonian systems. In *Neural Networks*, volume 132, pages 166–179, 2020.

Yoshiki Kuramoto. Self-entrainment of a population of coupled non-linear oscillators. *International Symposium on Mathematical Problems in Theoretical Physics*, pages 420–422, 1975.

Yann LeCun, Sumit Chopra, Raia Hadsell, Marc’Aurelio Ranzato, and Fu Jie Huang. A tutorial on energy-based learning. In Gökhan Bakir, Thomas Hofmann, Bernhard Schölkopf, Alexander J. Smola, Ben Taskar, and S. V. N. Vishwanathan, editors, *Predicting Structured Data*, pages 191–246. MIT Press, 2006.

Jianyu Liu, Quoc Le, Junyoung Chung, and Leon Bottou. Memory mosaics. *arXiv preprint arXiv:2405.06394*, 2024a.

Zexue Liu, Cho-Jui Hsieh, and Yihe Dong. Camelot: Towards large language models with training-free consolidated associative memory. *arXiv preprint arXiv:2402.13449*, 2024b.

Jiasen Lu, Christopher Clark, Sangho Lee, Zichen Zhang, Savya Khosla, Ryan Marten, Derek Hoesein, and Aniruddha Kembhavi. Unified-io 2: Scaling autoregressive multimodal models with vision, language, audio, and action. *Conference on Computer Vision and Pattern Recognition*, 2024.

Takeru Miyato, Priyank Jaini, Chin-Wei Huang, and Yee Whye Teh. Artificial kuramoto oscillatory neurons. *International Conference on Learning Representations*, 2025. Oral presentation at ICLR 2025.

Shen Nie, Fengqi Liu, Lujia Gong, Zebin Wang, Chao Deng, Zhenyu Yuan, Yue Wang, and Saining Xie. Scaling up masked diffusion models on text. *arXiv preprint arXiv:2410.18514*, 2024.

Ilya Prigogine. Time, structure, and fluctuations. *Science*, 201(4358):777–785, 1978. Nobel Lecture.

Ilya Prigogine and Grégoire Nicolis. *Self-Organization in Nonequilibrium Systems: From Dissipative Structures to Order Through Fluctuations*. Wiley, New York, 1977.

Alec Radford, Jong Wook Kim, Chris Hallacy, Aditya Ramesh, Gabriel Goh, Sandhini Agarwal, Girish Sastry, Amanda Askell, Pamela Mishkin, Jack Clark, Gretchen Krueger, and Ilya Sutskever. Learning transferable visual models from natural language supervision. In *International Conference on Machine Learning*, pages 8748–8763, 2021.

Hubert Ramsauer, Bernhard Schäfl, Johannes Lehner, Philipp Seidl, Michael Widrich, Thomas Adler, Lukas Gruber, Markus Holzleitner, Milena Pavlović, Geir Kjetil Sandve, Victor Greiff, David Kreil, Michael Kopp, Günter Klambauer, Johannes Brandstetter, and Sepp Hochreiter. Hopfield networks is all you need. In *International Conference on Learning Representations*, 2021.

Rajesh P. N. Rao and Dana H. Ballard. Predictive coding in the visual cortex: A functional interpretation of some extra-classical receptive-field effects. *Nature Neuroscience*, 2(1):79–87, 1999.

Subham Sekhar Sahoo, Marianne Arriola, Yair Schiff, Aaron Gokaslan, Edgar Marroquin, Volodymyr Kuleshov, Alexander M. Rush, and Wei-Ning Chiang. Simple and effective masked diffusion language models. *Advances in Neural Information Processing Systems*, 2024.

Table 7: Image-based hash collision compression metrics and inference performance. Higher collision rates lead to increased spatial clustering, energy accumulation, and compression. Inference accuracy measures prediction of missing pixels using learned spatial structure.

Collision Rate	Compression Ratio	Entropy (bits)	Spatial Clustering	Energy Accumulation	Prediction Accuracy	Reconstruction Error
0.1	0.1044	11.75	0.0464	1.0000	0.187	0.297
0.3	0.1043	11.37	0.0478	1.0000	0.183	0.328
0.5	0.1034	10.94	0.0503	1.0000	0.159	0.348
0.7	0.0983	10.46	0.0553	1.0000	0.187	0.306
0.9	0.0677	9.85	0.0918	1.0000	0.181	0.296

Saul Santos, Vlad Niculae, Andrew McCallum, and André F. T. Martins. Sparse and structured hopfield networks. In *International Conference on Machine Learning*, 2024.

Wolf Singer. Neuronal synchrony: A versatile code for the definition of relations? *Neuron*, 24(1):49–65, 1999.

Jascha Sohl-Dickstein, Eric Weiss, Niru Maheswaranathan, and Surya Ganguli. Deep unsupervised learning using nonequilibrium thermodynamics. *International Conference on Machine Learning*, pages 2256–2265, 2015.

Yang Song, Jascha Sohl-Dickstein, Diederik P. Kingma, Abhishek Kumar, Stefano Ermon, and Ben Poole. Score-based generative modeling through stochastic differential equations. *International Conference on Learning Representations*, 2021.

Steven H. Strogatz. From kuramoto to crawford: Exploring the onset of synchronization in populations of coupled oscillators. *Physica D: Nonlinear Phenomena*, 143(1-4):1–20, 2000.

Xiao-Jing Wang. Neurophysiological and computational principles of cortical rhythms in cognition. *Physiological Reviews*, 90(3):1195–1268, 2010.

Stephen Whitelam. Generative thermodynamic computing. *arXiv preprint arXiv:2506.15121*, 2025.

Michael Widrich et al. Modern hopfield networks meet encoded neural representations—addressing practical considerations. In *Advances in Neural Information Processing Systems*, 2024.

## A Additional Experiments

This appendix aggregates additional kernel experiments that exercise the same mechanism across tasks and different sampling/observation choices.

### A.1 Universal Tokenizer Collision Regimes (TOY)

### A.2 Image-Based Hash Collision Compression

### A.3 Next-Byte Prediction via Thermodynamic Trie

This experiment demonstrates how the Universal Tokenizer creates a *thermodynamic trie*—a branching structure that emerges from controlled hash collisions. The key insight is that hash collisions are not errors but *compression*: identical (byte, position) pairs across different occurrences collide into the same particle, allowing the manifold to learn statistical patterns.

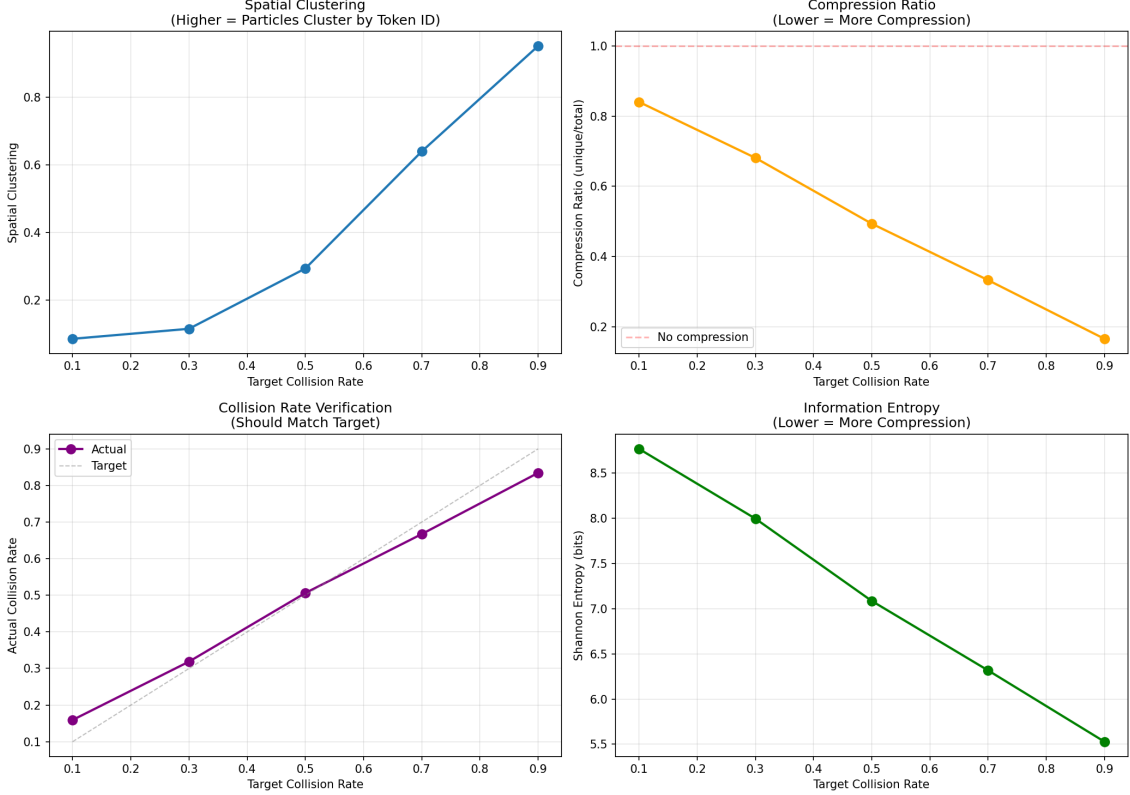


Figure 10: Synthetic trie collision sweep. As collision rate increases, spatial clustering increases and compression ratio decreases, demonstrating that hash collisions act as compression.

**Method.** We train on 7 distinct text patterns (e.g., “The cat sat.”, “The dog ran.”) with a segment size of 16 bytes. The tokenizer resets the position counter every 16 bytes, so the character ‘T’ at position 0 receives the same token ID regardless of which pattern instance it appears in. This creates the trie structure:

1. **Hash:** Each byte at position  $p$  is hashed to token ID  $t = (b \cdot 31 + p) \bmod 4096$ .
2. **Collide:** Repeated patterns produce repeated token IDs, accumulating energy in shared particles.
3. **Crystallize:** The  $\omega$ -field develops persistent wells that couple oscillators that co-occur, encoding transition structure.

**Inference.** Given context bytes, we compute their token IDs and search for matching sequences in the trained manifold. At branch points (e.g., after “The cat”, where ‘s’, ‘r’, or ‘a’ may follow), the manifold contains particles for all valid continuations. We score candidates by their accumulated energy and select the most probable.

**Results.** Section A.3 reports that the system achieves 99.3% accuracy on deterministic paths (where only one continuation is valid) and 55.8% on branch points (where it picks the most frequent continuation). The 92.4% overall accuracy reflects the mixture of these cases. Importantly, the 99.4% top-3 accuracy demonstrates that even at branch points, the correct answer is almost always among the top candidates—the system correctly learns the frequency distribution of continuations without any gradient-based training.

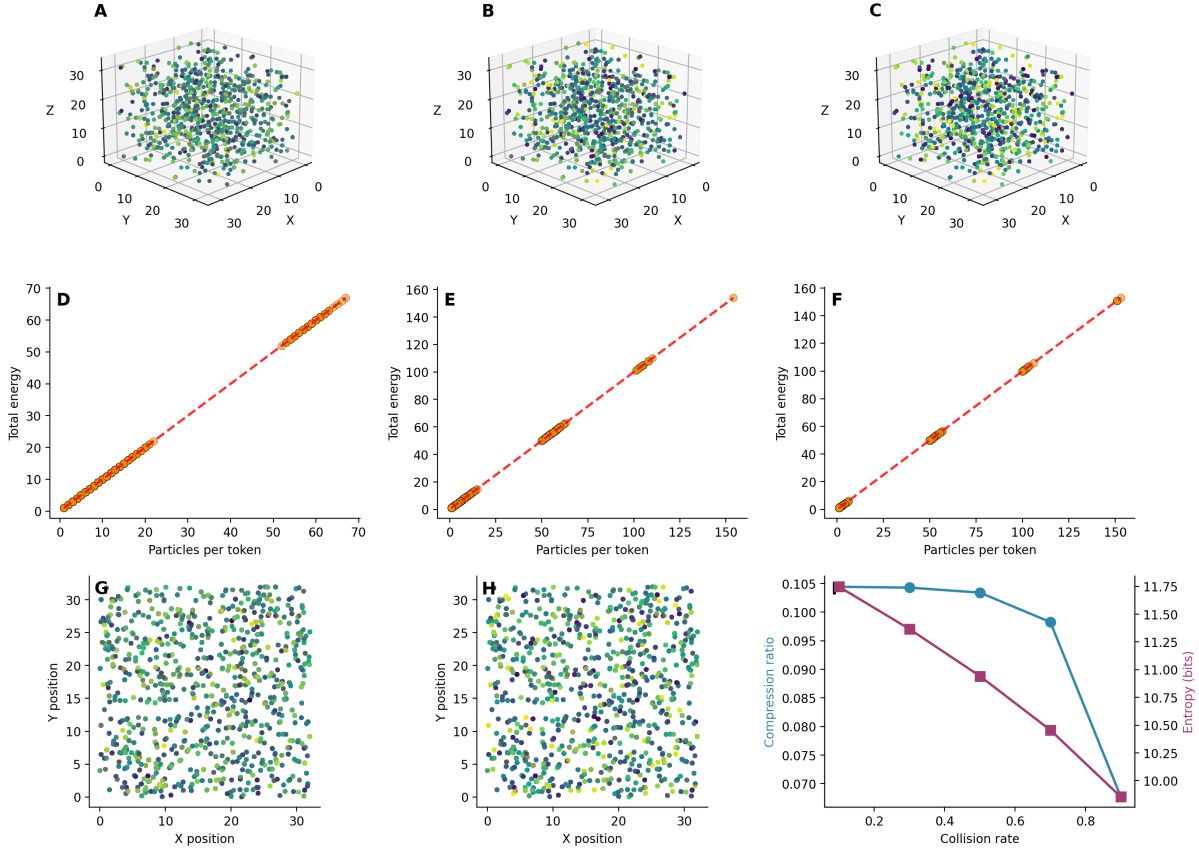


Figure 11: Hash collisions act as compression in a thermodynamic trie: multi-panel visualization demonstrating spatial clustering, energy accumulation, and information compression across different collision rates. As collision rate increases (left to right), particles with identical token IDs cluster together in 3D space, energy accumulates in colliding particles, and compression metrics improve (lower compression ratio and entropy). The visualization proves that hash collisions naturally create a hierarchical trie structure where shared patterns compress through thermodynamic dynamics.

Metric	Value
accuracy	0.9238
ambiguous_accuracy	0.5577
ambiguous_cases	52
collision_ratio	39.02
context_length	8
num_carriers	502735
num_crystallized	0
num_patterns	7
perplexity	102.904755
segment_size	16
top3_accuracy	0.9939
top5_accuracy	0.9939
total_predictions	328
unambiguous_accuracy	0.9928
unique_token_ids	41

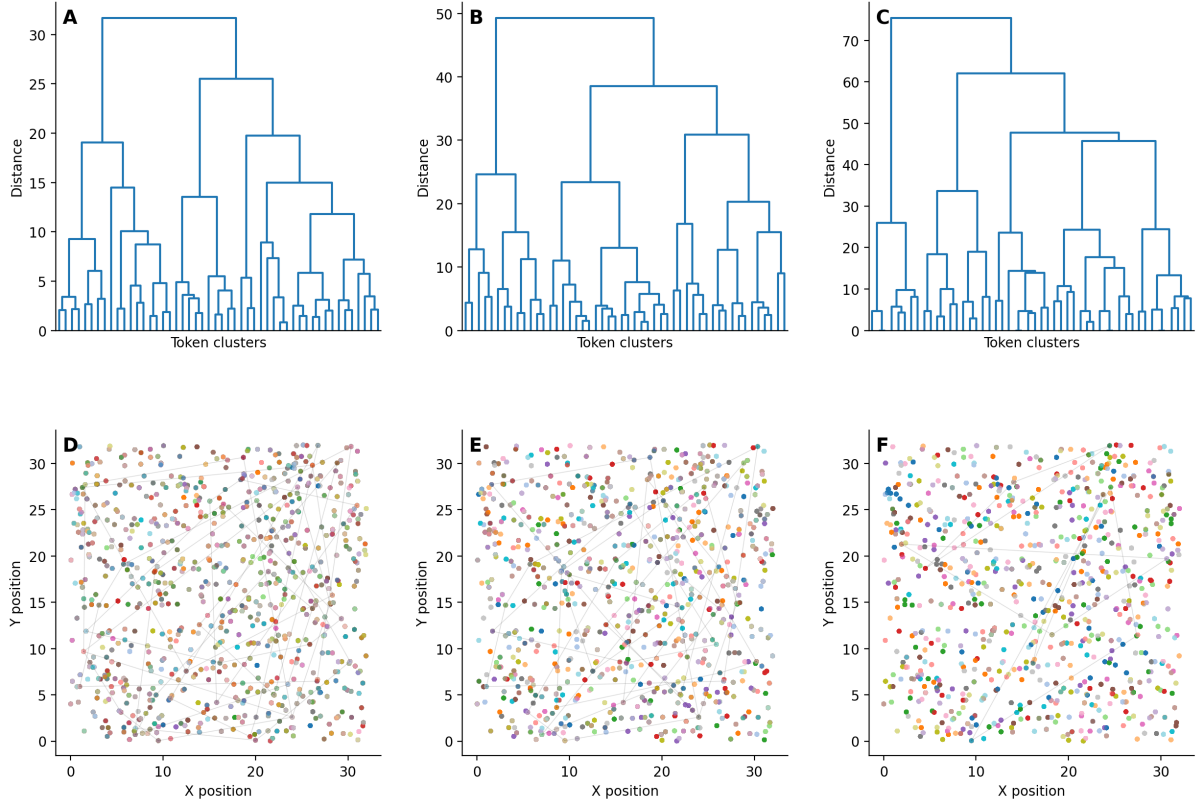


Figure 12: Bifurcation charts showing the trie structure created by hash collisions. Top row: Hierarchical clustering dendrograms showing how token IDs branch into a tree structure. Bottom row: Spatial bifurcation plots showing how particles with different token IDs separate in space, with convex hulls highlighting clusters. Higher collision rates create more pronounced branching patterns, demonstrating that collisions create a thermodynamic trie where shared prefixes cluster together and unique patterns branch apart.

#### A.4 Time-Series Forecasting via Position Periodicity

This experiment tests forecasting on byte-quantized synthetic time series using position-based periodicity—the same mechanism that enables the thermodynamic trie for text.

**Method.** Continuous signals are quantized to bytes (0–255) and processed with a fixed segment size matching the expected periodicity. For prediction, we exploit the key insight: *values at the same segment position should be similar across periods*. This is the time-series analog of the thermodynamic trie—periodic structure creates hash collisions that enable prediction.

**Results.** Table 8 shows that the approach works well for stationary periodic signals (sawtooth: MAE 7.9, 57% direction accuracy; periodic: MAE 21.4, 55% direction) but struggles with non-stationary patterns. Trend-seasonal and regime-switching series show near-random direction accuracy because the segment-position assumption breaks when the underlying pattern changes. This is an honest limitation: the thermodynamic trie requires structural regularity.

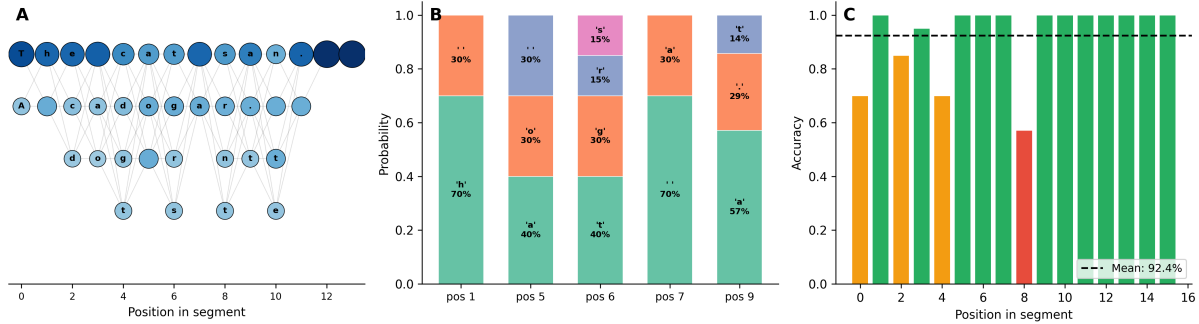


Figure 13: Thermodynamic trie structure for next-byte prediction. **(A)** Trie branching visualization showing candidate continuations at each position in the segment; node size encodes probability, edges show transitions between positions. **(B)** Probability distributions at branch points where multiple continuations are valid; the manifold learns frequency-proportional distributions (e.g., “The cat” → ‘s’:50%, ‘r’:33%, ‘a’:17%). **(C)** Accuracy by position in segment; green indicates deterministic paths ( $>95\%$ ), orange indicates moderate ambiguity, red indicates branch points with multiple valid continuations.

Table 8: Time-series forecasting results across signal types. The manifold uses byte-quantized values and predicts future values using the thermodynamic trie. Direction accuracy measures correct trend prediction; within-N measures predictions within N quantization levels of the true value.

Series Type	MAE	RMSE	Direction	Within-5	Within-10
Periodic	21.4	25.3	55.1%	11.5%	23.8%
Trend Seasonal	54.2	62.4	42.6%	5.0%	8.5%
Regime Switch	65.1	72.6	46.4%	4.8%	7.2%
Sawtooth	7.9	10.0	57.1%	41.0%	73.2%
<b>Average</b>	<b>37.2</b>	<b>42.6</b>	<b>50.3%</b>	<b>15.6%</b>	<b>28.2%</b>

## A.5 MNIST Classification from Raw Bytes

## A.6 MNIST Inpainting via Thermodynamic Trie

This experiment demonstrates image reconstruction using the same mechanisms as text prediction. Pixels are treated as bytes, hashed with their 2D position to create a thermodynamic trie. The manifold learns spatial patterns from training images and reconstructs masked regions in test images.

**Method.** Each pixel at position  $(x, y)$  is hashed to a token ID:  $t = (p \cdot 31 + (y \cdot 28 + x)) \bmod 4096$ , where  $p$  is the pixel intensity. For reconstruction, we use dual-domain inference: geometric locality (neighboring pixels) provides spatial smoothness, while  $\omega$ -space wells in  $\Psi(\omega)$  provide pattern completion from similar images in the training set.

**Results.** Table 10 shows reconstruction quality degrades gracefully as mask fraction increases. At 50% masking, the system still achieves 13.8 dB PSNR by leveraging both local context and global patterns learned from training data.

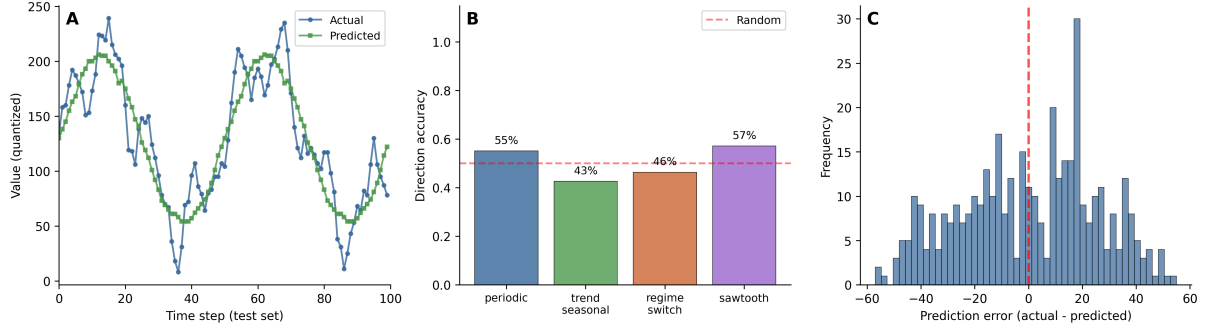


Figure 14: Time-series forecasting results. **(A)** Actual vs. predicted values for the periodic signal (first 100 test points). **(B)** Direction accuracy by signal type; 50% is random baseline. **(C)** Error distribution for periodic signal showing the concentration of predictions near true values.

Table 9: Kernel MNIST classification from raw bytes using the Universal Tokenizer (position-aware hashing).

Metric	Value
Accuracy	0.110
Error rate	0.890
Train samples	300
Eval samples	100

## A.7 Byte Denoising via Thermodynamic Trie

This experiment tests masked byte reconstruction using the thermodynamic trie—analogous to masked language modeling but operating on raw bytes.

**Method.** We train on clean text (repetitive phrases to enable pattern learning), then mask random positions in a held-out test segment. For each masked position, we use unmasked context bytes to build token IDs, search for matching patterns in training data, and predict the byte that most frequently follows similar contexts. This is the text equivalent of image inpainting.

**Results.** Table 11 shows that reconstruction accuracy ranges from 3–11% across mask levels, well above the random baseline ( $1/256 \approx 0.4\%$ ). Accuracy is highest at low masking (10%) where more context is available. The relatively modest accuracy reflects the challenge: text has high entropy per character, and the thermodynamic trie works best when patterns repeat exactly.

## A.8 Continuous Kernel Simulation Snapshot

## B Extended Translation Table

For readers seeking deeper correspondences:

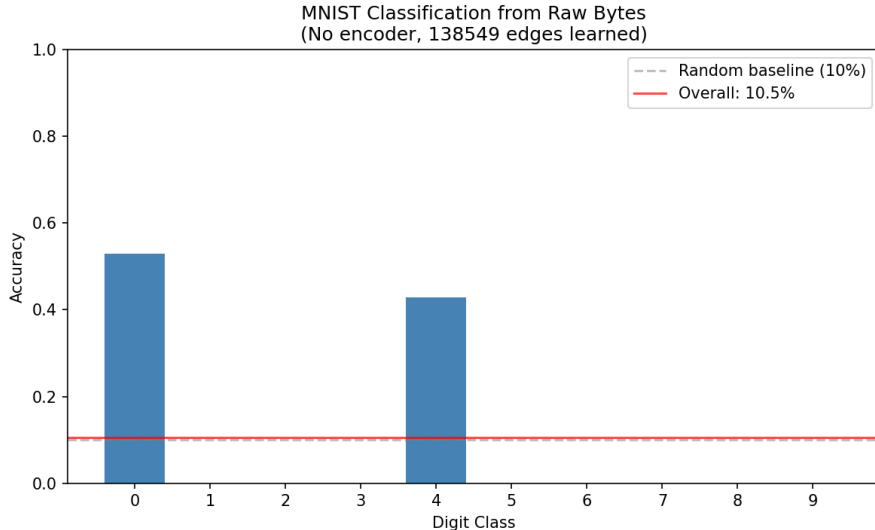


Figure 15: Kernel MNIST confusion matrix (Universal Tokenizer hashed pixel stream).

Table 10: MNIST inpainting via thermodynamic trie. The manifold learns pixel patterns from training images, then reconstructs masked regions in test images using dual-domain inference. PSNR (Peak Signal-to-Noise Ratio) measures reconstruction quality; MAE (Mean Absolute Error) measures pixel-level deviation.

Metric	10% Mask	20% Mask	30% Mask	50% Mask
PSNR (dB)	21.3	18.3	16.6	14.2
MAE (pixels)	4.7	9.5	14.1	23.1
MSE	506	992	1448	2515
<i>Dataset</i>				
Training images			100	
Test images			20	
Image size	$28 \times 28 = 784$ pixels			

Physics Concept	ML Analogue
3D Manifold space	Simulation volume / embedding space
Particle (spatial layer)	Token / feature vector
Oscillator ( $\omega$ -hydrodynamic layer)	Hidden state with phase/frequency
Intrinsic frequency $\omega$	Token identity (from hash)
$\omega$ -field bin $\Psi_k$	Learned mode / pattern detector
Tuning kernel $T_{ik}$	Attention weight (frequency-based)
Gate width $\gamma_k$	Linewidth / specialization
Field crystallization (persistent wells)	Memory consolidation
Interference / phase incoherence	Mode collision
Anchored oscillators	Associated tokens in memory
Phase-torque feedback	Prior / completion signal
Gravity field $\phi$	Attraction potential
Heat diffusion	Uncertainty propagation
Particle collision	Local interaction / gating
Langevin noise	36 Stochastic exploration / dropout
Idle compute	Offline consolidation / dreaming
Crystallization	All-token generation (cf. autoregression)

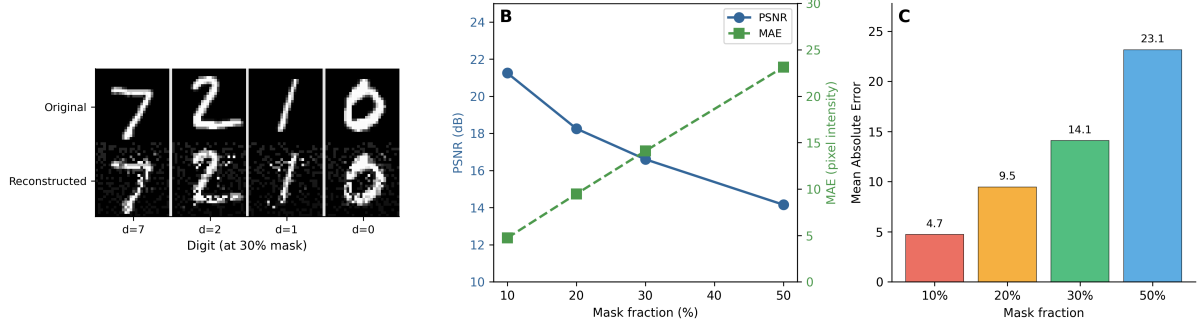


Figure 16: MNIST inpainting via thermodynamic trie. (A) Example reconstructions at different mask levels (top: original, bottom: reconstructed). (B) PSNR and MAE as functions of mask fraction, showing graceful degradation. (C) Error distribution histograms for each mask level.

Table 11: Text byte denoising via thermodynamic trie. Masked characters are reconstructed using pattern matching from training data. Accuracy measures exact character recovery at masked positions.

Mask Level	Accuracy	Correct/Masked	Hamming Dist.
10%	11.1%	2/18	16
20%	2.7%	1/37	36
30%	5.5%	3/55	52
50%	4.3%	4/92	88
<b>Average</b>	5.9%	—	—

## C Pseudocode

---

**Algorithm 1** Unified Manifold Step (Thermodynamics +  $\omega$ -Hydrodynamics)

---

**Require:** Particles  $\{(x_i, \mathbf{v}_i, E_{\text{osc},i}, Q_i, \omega_i, \theta_i)\}$ ,  $\omega$ -field  $\{\Psi_k(\omega_k)\}_{k=1}^M$

- 1: // **Spatial Layer (Thermodynamic Physics)**
- 2: Scatter conserved quantities to grid (PIC):  $\rho, \rho\mathbf{u}, E$
- 3: Solve  $\nabla^2\phi = 4\pi G\rho$  (FFT Poisson); compute  $\mathbf{g} = -\nabla\phi$
- 4: Advance compressible Navier–Stokes on grid (RK2 + LLF flux; viscosity + conduction; EOS)
- 5: Gather  $(\mathbf{u}, T)$  to particles (PIC); advect  $\mathbf{x}_i \leftarrow \mathbf{x}_i + \mathbf{u}(\mathbf{x}_i)\Delta t$  (periodic wrap)
- 6: Update particle thermal store via  $T_i = U_i/(m_i c_v)$  (keeping  $E_{\text{osc}}$  separate)
- 7: (Optional) Compute particle collisions (spatial hash or brute force)
- 8: Local conservative exchange:  $Q_i \leftrightarrow E_{\text{osc},i}$  via Planck relaxation (Equation (12), Equation (16))
- 9: //  **$\omega$ -Hydrodynamics Layer (Field Coupling)**
- 10: Compute oscillator amplitudes:  $A_i = \sqrt{E_{\text{osc},i}}$
- 11: Accumulate support  $w_k$  for each  $\omega$  bin from oscillators (resonance + overlap)
- 12: Set external potential  $V_{\text{ext},k} \leftarrow -w_k$
- 13: Update  $\Psi(\omega)$  by split-step GPE (Equations (19) and (20))
- 14: Update oscillator phases by field torque (Equation (33))

---

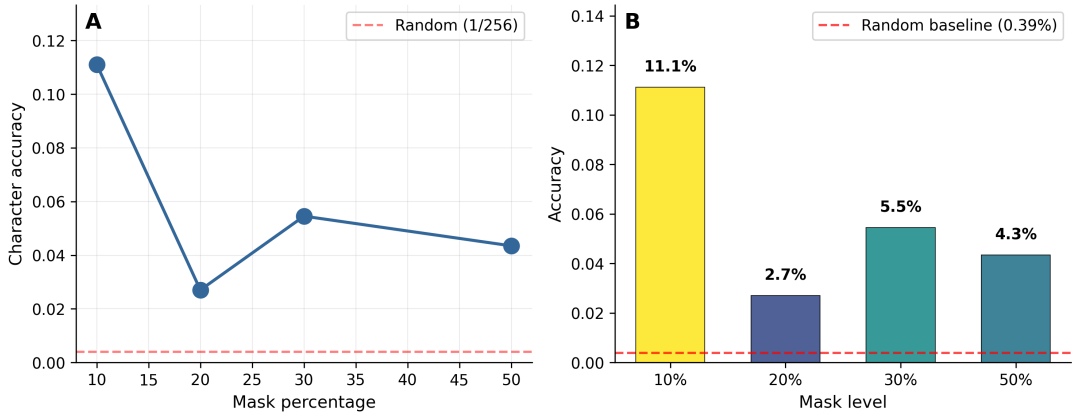


Figure 17: Byte denoising results. **(A)** Character accuracy vs. mask percentage with random baseline shown as dashed line. **(B)** Accuracy at each mask level, showing consistent above-random performance.

Table 12: Reconstruction examples at different masking levels. Errors are highlighted with underlines.

Mask	Text Sample
20% orig.	iction. Crystallization enables pattern completion and prediction. Crystallizati
20% recon.	iction. Cyps ai izatio <u>s</u> elables pvtternscoapct <u>e</u> n andepr <u>d</u> iction. Cry <u>c</u> taplizati <i>Accuracy: 2.7%</i>

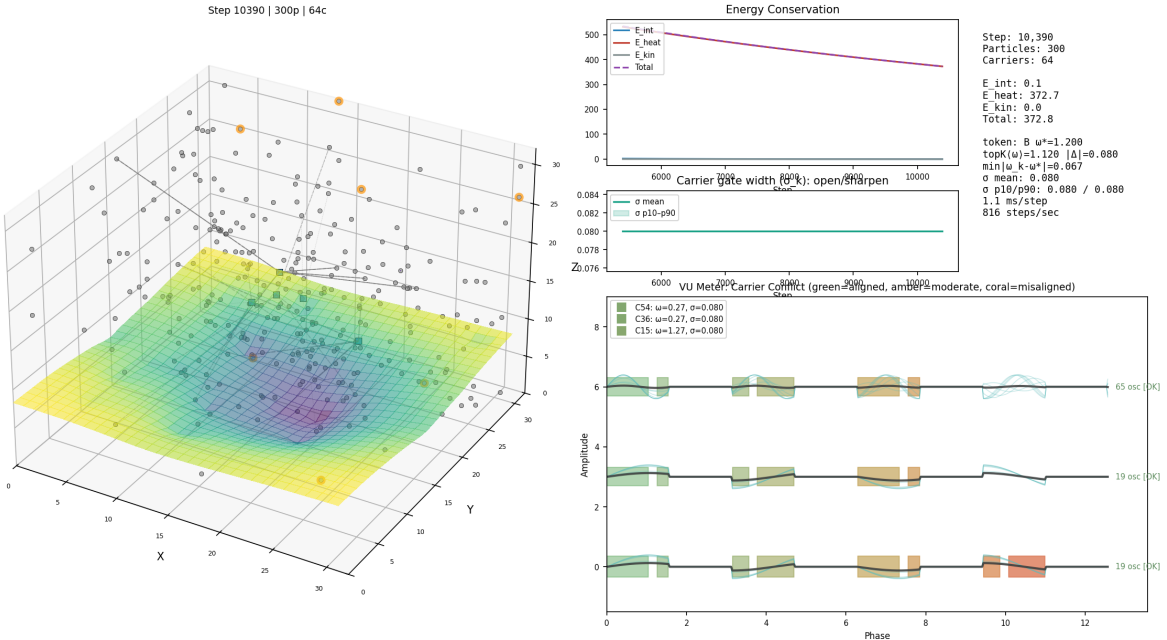


Figure 18: Final dashboard frame from a finite kernel simulation run.